

The Oxygen Abundance of Nearby Galaxies from Sloan Digital Sky Survey spectra

Leonid S. Pilyugin

*Main Astronomical Observatory of National Academy of Sciences of Ukraine, 27
Zabolotnogo str., 03680 Kiev, Ukraine*

pilyugin@mao.kiev.ua

and

Trinh X. Thuan

*Astronomy Department, University of Virginia, P.O. Box 400325, Charlottesville, VA
22904-4325*

txt@virginia.edu

ABSTRACT

We have derived the oxygen abundance for a sample of nearby galaxies in the Data Release 5 of the Sloan Digital Sky Survey (SDSS) which possess at least two independent spectra of one or several H II regions with a detected [OIII] λ 4363 auroral line. Since, for nearby galaxies, the [OII] λ 3727 nebular line is out of the observed wavelength range, we propose a method to derive (O/H)_{ff} abundances using the classic T_e method coupled with the ff relation. (O/H)₇₃₂₅ abundances have also been determined, based on the [OII] $\lambda\lambda$ 7320,7330 line intensities, and using a small modification of the standard T_e method. The (O/H)_{ff} and (O/H)₇₃₂₅ abundances have been derived with both the one- and two-dimensional t₂ – t₃ relations. It was found that the (O/H)_{ff} abundances derived with the parametric two-dimensional t₂ – t₃ relation are most reliable. Oxygen abundances have been determined in 29 nearby galaxies, based on 84 individual abundance determinations in H II regions. Because of our selection methods, the metallicity of our galaxies lies in the narrow range $8.2 \lesssim 12 + \log (O/H) \lesssim 8.4$. The radial distribution of oxygen abundances in the disk of the spiral galaxy NGC 4490 is determined for the first time.

Subject headings: galaxies: abundances – ISM: abundances – H II regions

1. INTRODUCTION

The chemical composition of a galaxy is one of its most fundamental characteristics. Because a galaxy’s chemical enrichment depends on various physical processes, such as the star formation history, the mass exchange between a galaxy and its environments and the stellar initial mass function, progress in our understanding of galaxy formation and evolution processes depends in large part upon improving our knowledge of the chemical properties of galaxies.

Relatively detailed studies of the chemical composition of the interstellar medium of galaxies can be carried out by using the emission lines in spectra of individual H II regions in nearby galaxies. However, such data is very limited. For example, spectra of individual H II regions in spiral galaxies have been obtained for only about five dozens objects (see the compilation in Pilyugin et al. (2004, 2007)). The Sloan Digital Sky Survey (York et al. 2000) provides a very large data base of galaxy spectra obtained in a homogeneous way, which allows to increase the number of abundance determinations in individual H II regions in nearby galaxies. The flux of the auroral oxygen line [OIII] λ 4363 is measurable in the SDSS spectra of many H II regions (Izotov et al. 2004, 2006; Kniazev et al. 2004). In those spectra, the electron temperature t_3 of the O^{++} zone can be measured directly. However, there is a problem concerning abundance determination of H II regions in nearby galaxies with SDSS spectra. The observed wavelength range is 3800 – 9300 Å so that for nearby galaxies with redshifts $z \lesssim 0.024$, the [OII] λ 3727 emission line is out of that range. The absence of the [OII] λ 3727 line prevents the use of the standard T_e method and of empirically or theoretically calibrated relations between metallicity and the relative fluxes of strong oxygen lines (Pagel et al. 1979; Edmunds & Pagel 1984; Dopita & Evans 1986; McCall et al. 1985; McGaugh 1991; Pilyugin 2000, 2001a; Pilyugin & Thuan 2005, among others) to determine oxygen abundances.

It has been suggested by Kniazev et al. (2003, 2004) that this problem can be solved by using a modification of the standard T_e method, based on the intensities of the [OII] $\lambda\lambda$ 7320,7330 auroral lines, instead of the intensity of the [OII] λ 3727 nebular line. In this modified version, the flux in the [OII] λ 3727 emission line is estimated from the fluxes of the [OII] $\lambda\lambda$ 7320,7330 emission lines and the $t_2 - t_3$ relation, where t_2 and t_3 are respectively the electron temperatures of the O^+ and O^{++} zones. However, the [OII] $\lambda\lambda$ 7320,7330 lines are weak and their measured fluxes usually have large errors, so that the O^+ abundances derived from those lines are generally not very accurate (Izotov et al. 2006). Furthermore, the difference between the t_2 temperature derived from the [OII] λ 3727/[OII] $\lambda\lambda$ 7320,7330 ratio and the one estimated from the commonly used $t_2 - t_3$ relation can be very large (see the discussion in Kennicutt et al. 2003, and references therein), making the oxygen abundances so derived

even more uncertain.

Recently, Pilyugin (2005); Pilyugin et al. (2006a) have derived a relation, called the ff relation, between the auroral $[\text{OIII}]\lambda 4363$ and nebular $[\text{OIII}]\lambda\lambda 4959, 5007$, $[\text{OII}]\lambda 3727$ oxygen line fluxes. Those authors showed that, by coupling the ff relation with the T_e method, accurate oxygen abundances can be derived from measurements of just two oxygen lines, $[\text{OIII}]\lambda\lambda 4959, 5007$ and $[\text{OII}]\lambda 3727$. Can the same combination of the ff relation and the T_e method yield also reliable oxygen abundances when only measurements of the two $[\text{OIII}]\lambda\lambda 4959, 5007$ and $[\text{OIII}]\lambda 4363$ oxygen lines are available? We will examine this question here. We will also look at the influence of the choice of a particular $t_2 - t_3$ relation on the derived abundances. After assessing the accuracy of the above method, we will use it to determine reliable oxygen abundances in a sample of nearby galaxies using SDSS spectra.

We describe the spectroscopic data set which forms the basis of the present investigation in Section 2. In Section 3, we discuss the methods used to determine oxygen abundances in galactic H II regions. In Section 4, we examine the reliability of the oxygen abundances determined in different ways, using the radial distribution of the oxygen abundance in the disk of the well-studied spiral galaxy M101 as a “Rosetta stone”. The oxygen abundances derived in a sample of nearby galaxies are discussed in Section 5. We summarize our conclusions in Section 6.

For the line fluxes, we will be using the following notations throughout the paper: $R_2 = I_{[\text{OII}]\lambda 3727 + \lambda 3729} / I_{H\beta}$, $R_3 = I_{[\text{OIII}]\lambda 4959 + \lambda 5007} / I_{H\beta}$, $R = I_{[\text{OIII}]\lambda 4363} / I_{H\beta}$, $R_{23} = R_2 + R_3$. With these definitions, the excitation parameter P can then be expressed as: $P = R_3 / (R_2 + R_3)$.

2. THE DATA

2.1. The galaxy sample

We have extracted from the Data Release 5 (DR5) of the Sloan Digital Sky Survey (SDSS) spectra of nearby galaxies which satisfy the following three conditions: 1) For each galaxy, there exists at least two independent SDSS spectral measurements of one or several H II regions in it. This criterion allows us to compare the oxygen abundances determined independently and assess their reliability. If there are H II regions at different galactocentric distances, an abundance gradient can also be determined; 2) each H II region has a high metallicity, i.e. it has an oxygen abundance $12 + \log (\text{O}/\text{H}) \gtrsim 8.2$; and 3) each spectrum shows a $[\text{OIII}]\lambda 4363$ auroral line. The last two criteria select out galaxies that are suited to our adopted method of abundance determination, described below.

These three criteria select out about a hundred galaxies out of the original 750 000 spectra in the DR5. However, the final list, given in Table 1, includes only those galaxies which we judge to have reliable oxygen abundance determinations (our reliability tests are discussed in section 4.2), a total of 29 nearby galaxies. Table 1 gives the general characteristics of each galaxy. The first column gives its name. We have used the most widely used name for each galaxy. The other informations concerning each galaxy are taken from the Lyon/Meudon Extragalactic Database (LEDa) and/or from the NASA/IPAC Extragalactic Database (NED). The right ascension and declination (J2000.0) of each galaxy are given in column 2, its morphological type and morphological type code in columns 3 and 4, its apparent B magnitude in column 5, its redshift in column 6, and its absolute blue magnitude in column 7. A Hubble constant of $73 \text{ km s}^{-1} \text{ Mpc}^{-1}$ has been adopted to convert from redshift to distance. Other designations of the galaxy are given in column 8.

Examination of Table 1 shows that our sample includes mainly late-type spirals and irregular galaxies. Several galaxies do not possess a published morphological type. The majority of the galaxies in the sample have a redshift less than 0.01, i.e. a distance less than $\sim 45 \text{ Mpc}$. The most distant galaxy in our list, HS1103+4346, has a redshift of 0.021 that corresponds to a distance of $\sim 90 \text{ Mpc}$. Their B absolute magnitudes range between -21.5, typical of spiral galaxies, and -16.5, typical of dwarf irregular galaxies.

2.2. The line intensity data

The line intensities of the H II regions in our sample of nearby galaxies have been derived using SDSS spectra in the following way, as illustrated by the following example concerning the H α line.

The continuum flux level in the wavelength range from $\lambda_a = 6500 \text{ \AA}$ to $\lambda_b = 6650 \text{ \AA}$ is approximated by the linear expression

$$f_c(\lambda) = c_0 + c_1\lambda. \quad (1)$$

The values of the coefficients in Eq.(1) are derived by an iteration procedure. In the first step, we exclude the H α line region, from 6540 \AA to 6590 \AA , and use all other data points to derive a first set of coefficients, using the least-squares method. Then, the point with the largest deviation is rejected, and a new set of coefficients is derived. The iteration procedure is continued until the differences between two successive values of $f_c(\lambda_a)$ and $f_c(\lambda_b)$ are respectively less than $0.01f_c(\lambda_a)$ and $0.01f_c(\lambda_b)$.

The profile of each line is approximated by a Gaussian of the form

$$f(\lambda) = F \frac{1}{\sqrt{2\pi}\sigma} e^{-(\lambda-\lambda_0)^2/2\sigma^2} \quad (2)$$

where λ_0 is the line central wavelength, σ is the width of the line, and F is the flux in the emission line. If there is a broad emission, such as in the spectrum # 1324-53088-234 shown in Fig. 1 of an H II region in the disk of the spiral galaxy M101, then several lines are fitted simultaneously. In this case, the total flux at a fixed value of λ is given by the expression

$$f(\lambda) = f_{H\alpha,narrow}(\lambda) + f_{H\alpha,broad}(\lambda) + f_{[NII]\lambda 6548}(\lambda) + f_{[NII]\lambda 6584}(\lambda) + f_c(\lambda) \quad (3)$$

The values of $F(H\alpha, narrow)$, $\lambda_0(H\alpha, narrow)$, $\sigma(H\alpha, narrow)$, $F(H\alpha, broad)$, $\lambda_0(H\alpha, broad)$, $\sigma(H\alpha, broad)$, $F([NII]\lambda 6548)$, $\lambda_0([NII]\lambda 6548)$, $\sigma([NII]\lambda 6548)$, $F([NII]\lambda 6584)$, $\lambda_0([NII]\lambda 6584)$, $\sigma([NII]\lambda 6584)$ are derived by requiring that the mean difference

$$\epsilon = \sqrt{\frac{1}{n} \sum_{k=1}^{k=n} (f(\lambda_k) - f^{obs}(\lambda_k))^2} \quad (4)$$

between the measured flux $f^{obs}(\lambda_k)$ and the flux $f(\lambda_k)$ given by Eq.(3) to be minimum in the range $\lambda_a - \lambda_b$. The derived fit to the $H\alpha$, $[NII]\lambda 6548$ and $[NII]\lambda 6584$ lines is shown by the solid line in Fig. 1. A similar procedure is adopted in the cases of broad absorption components or of partly overlapping lines.

The measured emission fluxes F are then corrected for interstellar reddening using the theoretical $H\alpha$ to $H\beta$ ratio and the analytical approximation to the Whitford interstellar reddening law from Izotov et al. (1994). In a few cases, the derived value of the extinction $C(H\beta)$ is negative and is set to zero.

The value of ϵ (Eq. 4) can be considered as an estimate of the uncertainty in the measurement of the flux in a 1 Å spectral interval. Since the total width of line is approximately equal to 4σ , the uncertainty in the line intensity measurement can be estimated as $dF = 4\sigma\epsilon$.

3. ABUNDANCE DETERMINATION

3.1. The standard $(O/H)_{st}$ abundances

To convert line intensities into abundances, we adopt a two-zone model for the temperature structure within the H II region. We follow the procedures of Izotov et al. (2006)

who have recently published a set of equations for the determination of oxygen abundances in H II regions, based on a five-level atom model. According to those authors, the electron temperature t_3 within the [O III] zone, in units of 10^4K , is given by the following equation

$$t_3 = \frac{1.432}{\log(R_3/R) - \log C_T} \quad (5)$$

where

$$C_T = (8.44 - 1.09 t_3 + 0.5 t_3^2 - 0.08 t_3^3) v \quad (6)$$

$$v = \frac{1 + 0.0004 x_3}{1 + 0.044 x_3} \quad (7)$$

and

$$x_3 = 10^{-4} n_e t_3^{-1/2}. \quad (8)$$

As for the ionic oxygen abundances, they are derived from the following equations

$$12 + \log(O^{++}/H^+) = \log(R_3) + 6.200 + \frac{1.251}{t_3} - 0.55 \log t_3 - 0.014 t_3, \quad (9)$$

$$\begin{aligned} 12 + \log(O^+/H^+) &= \log(R_2) + 5.961 + \frac{1.676}{t_2} \\ &- 0.40 \log t_2 - 0.034 t_2 \\ &+ \log(1 + 1.35 x_2), \end{aligned} \quad (10)$$

or

$$\begin{aligned} 12 + \log(O^+/H^+) &= \log(I_{[OII]\lambda 7320 + \lambda 7330}/I_{H\beta}) \\ &+ 6.901 + \frac{2.487}{t_2} - 0.483 \log t_2 \\ &- 0.013 t_2 + \log(1 - 3.48 x_2), \end{aligned} \quad (11)$$

where

$$x_2 = 10^{-4} n_e t_2^{-1/2}. \quad (12)$$

Here n_e is the electron density in cm^{-3} . The determination of the electron temperature t_2 will be discussed in detail in Section 4.

The total oxygen abundances are then derived from the following equation

$$\frac{O}{H} = \frac{O^+}{H^+} + \frac{O^{++}}{H^+}. \quad (13)$$

The oxygen abundances so derived from the measured R_3 and R_2 line intensity ratios, using Eqs.(9) and (10), will be referred to hereafter as $(O/H)_{\text{st}}$ standard abundances.

3.2. The $(\text{O}/\text{H})_{7325}$ abundances

As mentioned before, because the SDSS spectra cover the 3800 – 9300Å spectral range, the $[\text{OII}]\lambda 3727$ emission line is out of the observed range for galaxies with redshifts $z \lesssim 0.024$. In those cases, O^+/H^+ cannot be determined by the standard method, using Eq.(10). To get around that problem, Kniazev et al. (2003, 2004) have suggested a slight modification of the standard method. From very general considerations, it is expected (Aller 1984) that the O^+/H^+ abundance can equally well be derived from the intensities of the $[\text{OII}]\lambda\lambda 7320, 7330$ auroral lines, using Eqs.(9) and (11). Kniazev et al. (2004) found that this modified method works well over the range of abundances studied by them. We will refer to abundances derived by that method as $(\text{O}/\text{H})_{7325}$ abundances.

Kennicutt et al. (2003) have used respectively the $[\text{OIII}]\lambda 4363/[\text{OIII}]\lambda\lambda 4959, 5007$ and $[\text{OII}]\lambda\lambda 7320, 7330/[\text{OII}]\lambda 3727$ auroral to nebular line intensity ratios to derive the electron temperatures t_3 and t_2 for a number of relatively high-metallicity H II regions. Comparing t_2 to t_3 , they found the surprising result that the two temperatures are uncorrelated for most of the objects in their sample. They noted that, while the cause of the absence of correlation is not known, a possible reason is the contribution of recombination processes to the population of the level giving rise to the $[\text{OII}]\lambda\lambda 7320, 7330$ lines. On the other hand, Izotov et al. (2006) found a correlation between the t_2 and t_3 they derived from the above ratios for a sample of low-metallicity H II regions. Their $t_2 - t_3$ relation follows the one predicted by photoionization models, but the scatter of the data points is large. Izotov et al. (2006) attributed the large scatter to substantial flux errors of the weak $[\text{O II}]\lambda 7320 + \lambda 7330$ emission lines. These investigations suggest that the O^+/H^+ abundances derived from the intensities of the auroral lines $[\text{OII}]\lambda\lambda 7320, 7330$, using Eq.(11), are somewhat uncertain.

3.3. The $(\text{O}/\text{H})_{\text{ff}}$ abundances

The spectra of high-metallicity H II regions generally exhibit strong $[\text{OII}]\lambda 3727$ and $[\text{OIII}]\lambda 4959, 5007$ nebular lines, i.e. large R_2 and R_3 line intensity ratios. However, the $[\text{OIII}]\lambda 4363$ auroral line is generally not detected, i.e. R cannot be measured directly. This prevents the use of the T_e method for abundance determination. However, Pilyugin (2005); Pilyugin et al. (2006a) have established a relation – called the ff relation – of the form $R = f(R_2, R_3)$. Using this relation, the intensity of the auroral line can be estimated if measurements of the two nebular lines are available.

For the H II regions in our sample, the R and R_3 ratios can be measured directly from the SDSS spectra. But we have seen that for those galaxies with a redshift less than 0.024, the

[OII] λ 3727 is out of the observed spectral range, and R_2 is not directly available. However, since there is relation of the type $R = f(R_2, R_3)$, there must also be a relation of the type $R_2 = f(R, R_3)$, i.e. R_2 can be estimated if measurements of R and R_3 are available. Using the same 31 calibrating H II regions employed by Pilyugin et al. (2006a) to establish their $R = f(R_2, R_3)$ relation, we have derived the following relation

$$\begin{aligned} \log R_{2,ff} &= 2.98 - 0.44 \log R_3 - 1.01 (\log R_3)^2 \\ &+ 1.37 \log R + 0.14 (\log R)^2. \end{aligned} \quad (14)$$

Thus, we will use Eq.(14) to estimate R_2 and then determine the oxygen abundance with the help of Eqs. 9 and (10). The oxygen abundance derived in this way will be referred to as $(O/H)_{ff}$.

4. OXYGEN ABUNDANCES IN THE SPIRAL GALAXY M101: A COMPARISON OF O ABUNDANCES DERIVED BY DIFFERENT METHODS

We focus here our attention on the Sc spiral galaxy M101 = NGC 5457. This galaxy has long served as the prototype system for studying radial oxygen abundance gradients in spiral disks. Many spectroscopic studies of H II regions in the disk of M101 have been carried out (Smith 1975; Shields & Searle 1978; Rayo et al. 1982; McCall et al. 1985; Torres-Peimbert et al. 1989; Garnett & Kennicutt 1994; Kinkel & Rosa 1994; Kennicutt & Garnett 1996; van Zee et al. 1998; Garnett et al. 1999; Luridiana et al. 2002; Kennicutt et al. 2003; Bresolin 2007). As a result, there are in the literature some 40 measurements of H II regions in the disk of M101 with a detected [OIII] λ 4363 line, and the radial oxygen abundance gradient in the spiral galaxy is well established (Kennicutt et al. 2003; Pilyugin 2001b; Pilyugin et al. 2004). This abundance of data allows us to test the reliability of the oxygen abundances derived from the SDSS spectra, using different methods.

4.1. Comparison between the 1- and 2-dimensional t_2 – t_3 relations

The electron temperature t_2 is usually determined from a relation between t_2 to t_3 , derived by fitting H II region photoionization models. Several versions of this $t_2 - t_3$ relation have been proposed (Campbell et al. 1986; Garnett 1992; Pagel et al. 1992; Izotov et al. 1997; Deharveng et al. 2000; Oey & Shields 2000). In particular, a one-dimensional model-independent $t_2 - t_3$ relation has been proposed by Pilyugin et al. (2006b).

$$t_2 = 0.72 t_3 + 0.26 \quad (15)$$

Recently, Pilyugin (2007) has found evidence suggesting that, instead of a one-to-one correspondence between t_2 and t_3 , the $t_2 - t_3$ relation is also dependent on a second parameter, the excitation parameter P (defined in Section 1). Pilyugin (2007) has derived a two-dimensional parametric relation of the form

$$\frac{1}{t_2} = 0.41 \times \frac{1}{t_3} - 0.34 \times P + 0.81. \quad (16)$$

How do the above 1- and 2-dimensional $t_2 - t_3$ relations stand up to the available data for M101? Using Eqs.(9) and (10) together with the parametric $t_2 - t_3$ relation (Eq. (16)), we have computed standard oxygen abundances based on published observations of H II regions in the disk of M101 (Smith 1975; Shields & Searle 1978; Rayo et al. 1982; McCall et al. 1985; Torres-Peimbert et al. 1989; Garnett & Kennicutt 1994; Kinkel & Rosa 1994; Kennicutt & Garnett 1996; van Zee et al. 1998; Garnett et al. 1999; Luridiana et al. 2002; Kennicutt et al. 2003; Bresolin 2007). The derived $(O/H)_{st}$ abundances are shown by open circles in panel 1a of Fig.2, as a function of galactocentric radius normalized to the disk isophotal radius R_{25} . The galactocentric distances of the H II regions have been taken from Kennicutt & Garnett (1996). The solid line is the linear best fit to those data (42 points)

$$12 + \log(O/H) = 8.67 (\pm 0.03) - 0.71 (\pm 0.05) R_G/R_{25}. \quad (17)$$

The dotted lines show shifts of ± 0.1 dex from the best fit. The mean deviation of $\log(O/H)_{st}$ from the best fit is 0.073 dex.

We have then computed the standard oxygen abundances for the same sample of H II region spectra, but using the 1-dimensional $t_2 - t_3$ relation (Eq. (15)). The resulting $(O/H)_{st}$ abundances are shown by open circles as a function of galactocentric distance in panel 1b of Fig.2. Again, the solid line is the linear best fit to those data (42 points)

$$12 + \log(O/H) = 8.76 (\pm 0.04) - 0.85 (\pm 0.06) R_G/R_{25} \quad (18)$$

and the dotted lines are shifts of ± 0.1 dex from the best fit. The mean value of the deviations of $\log(O/H)_{st}$ from the best fit is 0.089 dex. Comparison between Eqs. (17) and (18) shows that the radial distributions of the standard oxygen abundances derived with the 1- and 2-dimensional $t_2 - t_3$ relations are rather similar. However, the scatter of the points in panel 1a obtained with the parametric relation is slightly lower than that in the diagram obtained with the one-dimensional relation. The agreement between the two diagrams is not surprising since the one-dimensional relation is just a kind of “average” of the parametric relation (Pilyugin 2007). Therefore, while the differences between the oxygen abundances derived with those relations can be appreciable for individual H II regions depending on their excitation level, the mean difference for a sample of H II regions with

different excitation parameters, varying in a random manner, should be near zero. We note that the one-dimensional relation derived by Pilyugin et al. (2006b) is close to the one proposed by Campbell et al. (1986) which has found wide acceptance and use. Consequently, the radial distributions of the standard oxygen abundances derived here with both the one-dimensional and parametric $t_2 - t_3$ relations are similar to the one found for the disk of M101 in previous studies:

$$12 + \log(O/H) = 8.76 (\pm 0.06) - 0.90 (\pm 0.08) R_G/R_{25} \quad (19)$$

(Kennicutt et al. 2003) (Eq. (5)) and

$$12 + \log(O/H) = 8.79 (\pm 0.03) - 0.88 (\pm 0.08) R_G/R_{25} \quad (20)$$

(Pilyugin et al. 2004) (Eq. (28)).

4.2. Comparison of O abundances derived by various methods

The [OIII] λ 4363 auroral line is seen in 20 SDSS spectra of H II regions in the disk of M101 (Fig.3). These spectra are listed in Table 2. The [OIII] λ 7320+ λ 7330 nebular lines are measurable in 19 of these spectra, allowing determination of $(O/H)_{7325}$. The only exception is spectrum # 1324-53088-236 (Fig.4). There must be some overlap between the SDSS targets and those of previous spectroscopic studies of H II regions in the disk of M101. However, we have not attempted cross-identifications because of the poor accuracy of the H II region positions used in previous studies. These positions generally come from the catalog of Hodge et al. (1990) and have uncertainties of 0.2-1 s of time in right ascension and 3-10 arcsec in declination. This means that two or more Hodge et al's objects can be within an error box of 1s-10 arcsec centered on the SDSS position, which may result in misidentifications.

The radial distribution of $(O/H)_{7325}$ abundances derived with the parametric $t_2 - t_3$ relation is shown by open circles in panel 2a of Fig.2. The solid and dotted lines in panel 2a are the same as in panel 1a. The mean deviation of $\log(O/H)_{7325}$ from the radial gradient traced by the standard abundances $(O/H)_{st}$ (Eq. (17)) is 0.124 dex. The dashed line is the linear best fit to the $(O/H)_{7325}$ data (17 data points)

$$12 + \log(O/H) = 8.58 (\pm 0.12) - 0.45 (\pm 0.25) R_G/R_{25}. \quad (21)$$

The galactocentric distances of the the H II regions have been computed from the coordinates associated with each spectrum and given in the SDSS database. The coordinates of the center of M101, its inclination and its position angle are from the Third Reference Catalog

of Bright Galaxies (de Vaucouleurs et al. 1991). The temperature t_2 can be derived from the parametric relation only if R_2 , and hence the excitation parameter P , can be determined. Since R_2 cannot be estimated from Eq. (14) for low-metallicity H II regions, then t_2 cannot be derived through the parametric $t_2 - t_3$ relation. Hence, in panel 2a of Fig.2, $(O/H)_{7325}$ abundances have been derived only for high-metallicity H II regions.

The radial distribution of $(O/H)_{7325}$ abundances derived with the one-dimensional $t_2 - t_3$ relation is shown by open circles in panel 2b of Fig.2. The solid and dotted lines in panel 2b are the same as in panel 1b. The mean deviation of $\log(O/H)_{7325}$ from the radial gradient traced by the standard abundances $(O/H)_{st}$ (Eq. (18)) is 0.195 dex. The dashed line is the linear best fit to the $(O/H)_{7325}$ data (17 data points; the two low-metallicity H II regions at the largest galactocentric distances were excluded)

$$12 + \log(O/H) = 8.53 (\pm 0.18) - 0.31 (\pm 0.38) R_G/R_{25}. \quad (22)$$

The radial distribution of $(O/H)_{ff}$ abundances derived with the parametric $t_2 - t_3$ relation is shown by open circles in panel 3a of Fig.2. The solid and dotted lines in panel 3a are the same as in panel 1a. The mean deviation of $\log(O/H)_{ff}$ from the radial gradient traced by the standard abundances $(O/H)_{st}$ (Eq. (17)) is 0.071 dex. The dashed line is the linear best fit to $(O/H)_{ff}$ data (18 data points)

$$12 + \log(O/H) = 8.68 (\pm 0.07) - 0.67 (\pm 0.14) R_G/R_{25}. \quad (23)$$

The $(O/H)_{ff}$ abundances have been derived from the 18 SDSS spectra with a detected $[OIII]\lambda 4363$ auroral line. Two spectra, 1324-53088-234 and 1323-52797-066, have been excluded because they pertain to H II regions at large galactocentric distances and hence with low-metallicity. Eq. (14) is not applicable in this regime, since it was derived only for H II regions with $12 + \log(O/H) \gtrsim 8.2$.

The radial distribution of $(O/H)_{ff}$ abundances derived with the one-dimensional $t_2 - t_3$ relation is shown by open circles in panel 3b of Fig.2. The solid and dotted lines in panel 3b are the same as in panel 1b. The mean deviation of $\log(O/H)_{ff}$ from the radial gradient traced by the standard abundances $(O/H)_{st}$ (Eq. (18)) is 0.082 dex. The dashed line is the linear best fit to $(O/H)_{ff}$ data (18 data points)

$$12 + \log(O/H) = 8.57 (\pm 0.07) - 0.48 (\pm 0.14) R_G/R_{25}. \quad (24)$$

Comparison between panels 1a and 3a of Fig.2 shows that the $(O/H)_{ff} - R_G$ and the $(O/H)_{st} - R_G$ diagrams derived with the parametric $t_2 - t_3$ relation are in good agreement, in the sense that the mean deviation of the $(O/H)_{ff}$ abundances (0.071 dex) from the radial trend

traced by the $(O/H)_{st}$ abundances is close to the mean deviation of the $(O/H)_{st}$ abundances (0.073 dex). The global characteristics of the radial distributions (the central abundance and the slope) of the $(O/H)_{ff}$ and $(O/H)_{st}$ abundances are also close to each other (compare Eq. (17) and Eq. (23)). It should be emphasized that the reliability of the determination of the global characteristics of the radial abundance distribution depends not only on the accuracy of the abundance determination in individual H II regions, but also on the range of galactocentric distances over which these H II regions are distributed. Indeed, if we consider the $(O/H)_{st}$ - R_G diagram only for H II regions in the inner part of the disk, with galactocentric distances R_G/R_{25} less than 0.6 (at this distance the value of $12 + \log(O/H)$ decreases to ≈ 8.2 , the lower limit for the applicability of our method for determining $(O/H)_{ff}$ abundances) then the linear best fit to the resulting 23 data points is

$$12 + \log(O/H) = 8.63 (\pm 0.08) - 0.59 (\pm 0.17) R_G/R_{25}. \quad (25)$$

It is worth noting that the agreement between the central abundance and the slope derived from $(O/H)_{st}$ abundances for H II regions in the inner part of the disk, Eq. (25), and those quantities derived from the same $(O/H)_{st}$ abundances, but for H II regions in the whole disk, Eq. (17), is worse than the agreement between the central abundance and the slope derived from $(O/H)_{ff}$ abundances for H II regions in the same inner part of the disk, Eq. (23), and those quantities derived from $(O/H)_{st}$ abundances for H II regions in the whole disk, Eq. (17).

Comparison between panels 1b and 3b of Fig.2 shows that the $(O/H)_{ff} - R_G$ and the $(O/H)_{st} - R_G$ diagrams derived with the one-dimensional $t_2 - t_3$ relation are in reasonable agreement, or at least they are not in conflict. The mean deviation of the $(O/H)_{ff}$ abundances from the radial trend traced by the $(O/H)_{st}$ abundances (0.082 dex) is close to the mean deviation of the $(O/H)_{st}$ abundances (0.089 dex). However, there appears to be a discrepancy between the global characteristics of the radial distribution of the $(O/H)_{ff}$ abundances and those of the $(O/H)_{st}$ abundances: they do not agree within the formal uncertainties (compare Eq. (18) with Eq. (24)). This suggests that there may exist a small systematic error in the $(O/H)_{ff}$ abundances. However, if we again consider the $(O/H)_{st}$ - R_G diagram only for H II regions in the inner part of the disk, then the linear best fit to the resulting 23 data points is

$$12 + \log(O/H) = 8.71 (\pm 0.10) - 0.74 (\pm 0.22) R_G/R_{25}, \quad (26)$$

Now the global characteristics of the radial distributions of the $(O/H)_{ff}$ and $(O/H)_{st}$ abundances agree within the formal uncertainties (compare Eq. (26) with Eq. (24)). Alternatively, if we add to our set of $(O/H)_{ff}$ abundances the data point corresponding to the H II region with the largest galactocentric distance ($R_G/R_{25} = 1.25$) in the set of $(O/H)_{st}$

abundances, then the linear best fit to this "extended" data set (19 data points) is

$$12 + \log(O/H) = 8.75 (\pm 0.05) - 0.82 (\pm 0.09) R_G/R_{25}. \quad (27)$$

Again, the global characteristics of the radial distributions of the $(O/H)_{\text{ff}}$ and $(O/H)_{\text{st}}$ abundances agree within the formal uncertainties (compare Eq. (27) with Eq. (24)). The fact that the $(O/H)_{\text{ff}}$ abundances, derived here with both the one-dimensional and parametric $t_2 - t_3$ relations, give a general radial trend close to the one traced by the $(O/H)_{\text{st}}$ abundances suggests that reasonably accurate $(O/H)_{\text{ff}}$ oxygen abundances can be derived for H II regions with oxygen abundances in the range $8.20 \lesssim 12 + \log(O/H) \lesssim 8.55$, when only $[\text{OIII}]\lambda 4959 + \lambda 5007$ and $[\text{OIII}]\lambda 4363$ line intensity measurements are available. However, a small systematic error in the $(O/H)_{\text{ff}}$ abundances derived with the one-dimensional $t_2 - t_3$ relation cannot be ruled out.

Comparison of panels 1a and 2a and of panels 1b and 2b in Fig.2 shows that the radial distribution of the $(O/H)_{7325}$ abundances follows the same general trend traced by the $(O/H)_{\text{st}}$ abundances. Examination of panels 1a, 2a, and 3a shows that the scatter in the $(O/H)_{7325} - R_G$ diagram is appreciably larger than the scatter in the $(O/H)_{\text{st}} - R_G$ and $(O/H)_{\text{ff}} - R_G$ diagrams. Comparison between panels 2a and 2b shows that the scatter in the $(O/H)_{7325} - R_G$ diagram is lower for the parametric $t_2 - t_3$ relation than the one-dimensional relation. This suggests that the parametric relation gives more accurate values of t_2 as compared to the one-dimensional relation. Fig.2 also shows that using the parametric relation instead of the one-dimensional one results in a significant decrease of the scatter in the $(O/H)_{7325} - R_G$ diagram, but only in a marginal one in the $(O/H)_{\text{st}} - R_G$ and $(O/H)_{\text{ff}} - R_G$ diagrams. This can be understood by the fact that the relation between the O^+/H^+ abundance and the $[\text{OII}]\lambda 7320 + \lambda 7330$ line intensity (Eq. (10)) has a stronger dependence on t_2 than the one between the O^+/H^+ abundance and the $[\text{OII}]\lambda 3727$ line intensity (Eq. (11)). Therefore, the same error in t_2 results in a larger error in the $(O/H)_{7325}$ abundances than in the $(O/H)_{\text{st}}$ and $(O/H)_{\text{ff}}$ abundances.

In summary, we have arrived at the following main conclusions: 1) reasonably accurate $(O/H)_{\text{ff}}$ abundances can be derived for H II regions with oxygen abundances in the range $8.20 \lesssim 12 + \log(O/H) \lesssim 8.55$, when only $[\text{OIII}]\lambda 4959 + \lambda 5007$ and $[\text{OIII}]\lambda 4363$ line intensity measurements are available; 2) there is a hint that the parametric $t_2 - t_3$ relation provides more accurate values of t_2 than the one-dimensional relation.

5. OXYGEN ABUNDANCES IN NEARBY GALAXIES

5.1. Abundances and abundance gradients

We have extracted from the Data Release 5 of the SDSS spectra of individual H II regions in about a hundred nearby galaxies which have the particularity of possessing two or more spectra of the same or different H II regions with a detected [OIII] λ 4363 line. We have determined the $(\text{O}/\text{H})_{\text{ff}}$ and $(\text{O}/\text{H})_{7325}$ abundances for each H II regions. The final list, given in Table 1, consists of 29 galaxies, with 84 individual oxygen abundance determinations. The following criteria have been used to select the objects in the final list: 1) their H II regions have high metallicities, i.e. $12 + \log (\text{O}/\text{H}) \gtrsim 8.20$, because Eq. (14) is only applicable in that metallicity range; 2) $(\text{O}/\text{H})_{\text{ff}}$ abundances derived from two or more SDSS spectra of the same H II region, when available, differ by less than 0.1 dex; and 3) the $(\text{O}/\text{H})_{\text{ff}}$ abundances of different H II regions within the same galaxy, but with similar galactocentric distances are consistent with each other, i.e. their abundances differ by less than 0.1 dex. Criteria 2 and 3 are designed to select only galaxies with reliably determined oxygen abundances. Those criteria were not applied to M101, in this case all the H II regions with measured [OIII] λ 4363 line were included in the consideration.

The measured line intensities and derived abundances for our sample of nearby galaxies are given in Table 2. For each galaxy, we give in column 2 the SDSS spectrum number, composed of the plate number, the modified Julian date of observations and the number of the fiber on the plate. The galactocentric distance normalized to the isophotal radius of the galaxy is listed in column 3. The galactocentric distances were obtained from the SDSS coordinates of the spectral observations. The coordinates of the center of each galaxy, its diameter, inclination and major axis position angle were taken from the Lyon/Meudon Extragalactic Database (LEDa) and the NASA/IPAC Extragalactic Database (NED). The dereddened intensities and uncertainties of the [OIII] λ 4363, [OIII] λ 4959+ λ 5007 and [OII] λ 7320+ λ 7330 lines are given respectively in columns 4, 5 and 6. The line intensities have been scaled so that $I_{H\beta} = 1$. The electron temperature t_3 within the O^{++} zone is shown in column 7. The $(\text{O}/\text{H})_{7325}$ and $(\text{O}/\text{H})_{\text{ff}}$ abundances determined with the parametric relation (Eq. (16)) are given respectively in columns 8 and 9, while the same abundances determined with the one-dimensional relation (Eq. (15)) are given respectively in columns 10 and 11.

Examination of Table 2 shows that the vast majority of the H II regions in our sample have oxygen abundances in the very narrow interval $8.2 \lesssim 12 + \log (\text{O}/\text{H}) \lesssim 8.4$. This narrow metallicity range is due to two selections effects. As noted before, H II regions with $12 + \log (\text{O}/\text{H}) \lesssim 8.2$ have been excluded because Eq. (14) is only applicable to high-metallicity H II regions. At the other metallicity end, the [OIII] λ 4363 line is too weak to be detected in

SDSS spectra of H II regions with $12+\log(\text{O}/\text{H}) \gtrsim 8.4$.

In our sample, there are two galaxies (besides M101), which each have five distinct H II region measurements with a detected [OIII] λ 4363 line. The first galaxy is NGC 4490, and its measured H II regions span a large enough range of galactocentric distances to allow a derivation of the metallicity radial distribution in its disk. Its $(\text{O}/\text{H})_{\text{ff}}$ and $(\text{O}/\text{H})_{7325}$ abundances derived with the parametric relation are shown respectively by open circles and plus signs as a function of galactocentric distance in the top panel of Fig.5. The solid line is the linear least-squares fit to the $(\text{O}/\text{H})_{\text{ff}}$ data:

$$12 + \log(\text{O}/\text{H}) = 8.33 (\pm 0.02) - 0.063 (\pm 0.082) R_G/R_{25} \quad (28)$$

The mean deviation is 0.017 dex. The dashed line is the linear least-squares fit to the $(\text{O}/\text{H})_{7325}$ data:

$$12 + \log(\text{O}/\text{H}) = 8.39 (\pm 0.04) - 0.154 (\pm 0.165) R_G/R_{25} \quad (29)$$

The mean deviation is 0.035 dex.

The bottom panel shows a similar diagram, but with the $(\text{O}/\text{H})_{\text{ff}}$ and $(\text{O}/\text{H})_{7325}$ abundances derived with the one-dimensional relation. As in the top panel, the linear least-squares fit to the $(\text{O}/\text{H})_{\text{ff}}$ data is shown by the solid line:

$$12 + \log(\text{O}/\text{H}) = 8.37 (\pm 0.03) - 0.088 (\pm 0.101) R_G/R_{25} \quad (30)$$

The mean deviation is 0.021. The linear least-squares fit to the $(\text{O}/\text{H})_{7325}$ data is shown by the dashed line:

$$12 + \log(\text{O}/\text{H}) = 8.48 (\pm 0.06) - 0.243 (\pm 0.237) R_G/R_{25} \quad (31)$$

The mean deviation is 0.050.

The second galaxy is NGC 428. As for NGC 4490, the top panel of Fig.6 shows the $(\text{O}/\text{H})_{\text{ff}}$ and $(\text{O}/\text{H})_{7325}$ derived with the parametric relation as a function of galactocentric distance, while the bottom panel shows the same quantities derived with the one-dimensional relation. Unfortunately, the measured H II regions in NGC 428 cover a too small interval of galactocentric distances to allow a derivation of the radial distribution of oxygen abundances across the disk of the galaxy. We can however estimate the mean value of the oxygen abundance within a small range of galactocentric distances. The mean values are: $12+\log(\text{O}/\text{H})_{\text{ff}} = 8.33 \pm 0.03$ and $12+\log(\text{O}/\text{H})_{7325} = 8.33 \pm 0.08$, when determined with the parametric $t_2 - t_3$ relation. The mean values are: $12+\log(\text{O}/\text{H})_{\text{ff}} = 8.32 \pm 0.08$ and $12+\log(\text{O}/\text{H})_{7325} = 8.35 \pm 0.17$, when determined with the one-dimensional $t_2 - t_3$ relation. As in our study of

M101, we find that the scatter in $(\text{O}/\text{H})_{\text{ff}}$ abundances is smaller when determined with the parametric relation than when determined with the one-dimensional relation.

The scatter also increases when going from $(\text{O}/\text{H})_{\text{ff}}$ to $(\text{O}/\text{H})_{7325}$ abundances, even when both are determined with the same $t_2 - t_3$ relation. What is the origin of such an increase in scatter? From one point of view, we would expect the increase to be caused by measurement errors of the weak $[\text{OII}]\lambda 7320 + \lambda 7330$ emission lines. From another point of view, measurement errors of the $[\text{OIII}]\lambda 4363$ emission line can also be responsible for the differences between $(\text{O}/\text{H})_{\text{ff}}$ and $(\text{O}/\text{H})_{7325}$ abundances. Indeed, measurement errors of $[\text{OIII}]\lambda 4363$ result in errors in the t_3 temperature which, in turn, induces errors in the t_2 temperature. As noted above, the relation between O^+/H^+ and $[\text{OII}]\lambda 7320 + \lambda 7330$ is more strongly dependent on t_2 than the relation between O^+/H^+ and $[\text{OII}]\lambda 3727$ (compare Eq. (10) to Eq. (11)). Therefore, the same error in t_2 results in a larger error in the $(\text{O}/\text{H})_{7325}$ abundances than in the $(\text{O}/\text{H})_{\text{st}}$ and $(\text{O}/\text{H})_{\text{ff}}$ abundances which, in turn, causes differences between the $(\text{O}/\text{H})_{\text{ff}}$ and the $(\text{O}/\text{H})_{7325}$ abundances.

Thus measurement errors in $[\text{OIII}]\lambda 4363$ and $[\text{OII}]\lambda 7320 + \lambda 7330$ lines will both contribute to make the $(\text{O}/\text{H})_{\text{ff}}$ and the $(\text{O}/\text{H})_{7325}$ abundances determined with the same $t_2 - t_3$ relation differ from each other. Which contribution is greater? To answer that question, we have plotted in the top panel of Fig.7 $\Delta \log(\text{O}/\text{H}) = |\log(\text{O}/\text{H})_{\text{ff}} - \log(\text{O}/\text{H})_{7325}|$, where both abundances are determined with the parametric relation, against the fractional uncertainty in the measurement of the $[\text{OIII}]\lambda 4363$ emission line (the uncertainty in the line measurement expressed in units of the line intensity). In the bottom panel of Fig.7, we have plotted the same quantity against the fractional uncertainty in the measurement of the $[\text{OII}]\lambda 7320 + \lambda 7330$ emission lines. Inspection of the top panel of Fig.7 shows that the differences between $(\text{O}/\text{H})_{\text{ff}}$ and $(\text{O}/\text{H})_{7325}$ are small in H II regions with an accurate measurement of the $[\text{OIII}]\lambda 4363$ emission line, with an uncertainty of less than $\sim 10\%$. The maximum difference between $(\text{O}/\text{H})_{\text{ff}}$ and $(\text{O}/\text{H})_{7325}$ increases with increasing uncertainty in $[\text{OIII}]\lambda 4363$. The dotted line shows an eye fit to the maximum differences. However, the correlation between $\Delta(\text{O}/\text{H})$ and the $[\text{OIII}]\lambda 4363$ uncertainties is weak (dashed line). On the other hand, the H II regions that do have accurate $[\text{OII}]\lambda 7320 + \lambda 7330$ measurements, with an uncertainty less than 10%, still show large differences between $(\text{O}/\text{H})_{\text{ff}}$ and $(\text{O}/\text{H})_{7325}$ (bottom panel of Fig.7). This suggests that the differences between $(\text{O}/\text{H})_{\text{ff}}$ and $(\text{O}/\text{H})_{7325}$ abundances in our H II region sample are mainly due to measurement uncertainties in the $[\text{OIII}]\lambda 4363$ line, and hence, to uncertainties in the electron temperature determination.

5.2. Comparison of derived O abundances with previous work

5.2.1. The $t_2 - t_3$ relation

Some H II regions in our sample have independent oxygen abundance determinations by other authors (Kniazev et al. 2004; Izotov et al. 2006), based on the same SDSS spectra. They are listed in Table 3. In Fig.8, we compare our $(O/H)_{7325}$ abundances (labeled PT on the x-axis), derived with the one-dimensional $t_2 - t_3$ relation, with those obtained by Izotov et al. (2006) (labeled I on the y-axis) in the top panel, and with those derived by Kniazev et al. (2004) (labeled K on the y-axis) in the lower panel. The filled circles are individual H II regions from Table 3, and the solid lines correspond to equal abundances.

Inspection of Fig.8 and examination of Table 3 show that there are systematic differences between our $(O/H)_{7325}$ abundances and those obtained by the previously quoted authors, in the sense that our abundances are generally larger than theirs. The differences are especially large for the Kniazev et al.’s abundances (bottom diagram). Since the same SDSS spectra are used in all cases, the differences must be due to differences in abundance determination methods, in particular in the $t_2 - t_3$ relation used. Fig.9 shows the $t_2 - t_3$ relations used by us and the above authors. Open and filled circles denote H II regions with $[OIII]\lambda 4363$ and $[OII]\lambda 7320 + \lambda 7330$ line measurements with uncertainties less than 20%, with the t_2 temperature derived respectively from the parametric and one-dimensional $t_2 - t_3$ relation. The solid and dashed lines show the parametric relations respectively for two different values of the excitation parameter, $P = 0.5$ and 0.9 . The $t_2 - t_3$ relation of Izotov et al. (1994) used by Kniazev et al. (2004) is shown by crosses, while the one used by Izotov et al. (2006) is shown by plus signs. Fig.9 shows that there is a significant shift of the t_2 temperatures derived with our one-dimensional $t_2 - t_3$ relation (filled circles) as compared to those derived by Kniazev et al. (2004) (crosses). It is this shift which is responsible for the differences between our and Kniazev et al. (2004) $(O/H)_{7325}$ abundances. To illustrate this point directly, we have recomputed oxygen abundances for our H II region subsample with the $t_2 - t_3$ relation used by Kniazev et al. (2004). These abundances are plotted against our abundances computed with the one-dimensional relation as small plus signs in the bottom panel of Fig.8. The plus signs and the filled circles do indeed occupy the same general region.

5.2.2. The luminosity – metallicity relation

It is interesting to check how our derived oxygen abundances fit in the luminosity – central metallicity relation for galaxies, such as the one constructed by Pilyugin et al. (2007). Since for the majority of the galaxies in our sample, the abundances were derived at only

two galactocentric distances, the central metallicity can only be estimated for a handful of galaxies. We can estimate central metallicities for galaxies which satisfy one the following conditions: 1) the galaxy has at least one H II region at a galactocentric distance less than one tenth of the isophotal radius; or 2) it has a low-luminosity ($M_B \gtrsim -18$) and a morphological type Sm or later (i.e. the morphological type code given in Table 1 is higher than 8.0). It is known that the O/H distribution across the body of low-mass dwarf irregular galaxies does not show a gradient (Pagel et al. 1978; Devost et al. 1997). Then, the abundance in a H II region at any galactocentric distance is representative of the chemical composition of the dwarf galaxy’s interstellar medium as a whole. The galaxies so selected and for which a central metallicity can be estimated are listed in Table 4. The central oxygen abundance derived in the cases of both the parametric and one-dimensional $t_2 - t_3$ relations are shown for each galaxy respectively in columns 3 and 4. The central abundance, derived by extrapolating the linear fit in Fig. 5 to $R = 0$, is given for the galaxy NGC 4490, while the average value of the oxygen abundance is given for the other galaxies.

The luminosity – central metallicity diagram is shown in Fig.10. The open circles denote the galaxies in our sample (Table 4) with abundances determined with the parametric $t_2 - t_3$ relation in the upper panel, and with the one-dimensional relation in the bottom panel. The filled circles in both panels represent data from Pilyugin et al. (2007). Inspection of Fig.10 shows that the majority of the galaxies in our sample follow well the general trend of the luminosity – central metallicity relation. This can be considered as an indirect evidence in favour of the reliability of our abundance determinations. An exception is the spiral galaxy NGC 4490 which has an oxygen abundance too low for its luminosity. This galaxy is the only interacting galaxy among all galaxies listed in Table 4. This suggests that metal-poor gas infall may be responsible for its relatively low metallicity.

6. CONCLUSIONS

We have determined oxygen abundances for a sample of nearby galaxies in the Data Release 5 of the Sloan Digital Sky Survey, selected to possess two or more independent spectra of one or several H II regions with a detected [O III] $\lambda 4363$ emission line. Since the nebular [OII] $\lambda 3727$ line is out of the observed wavelength range in SDSS spectra of H II regions in nearby galaxies, we propose a method to determine $(O/H)_{ff}$ oxygen abundances, using the classic T_e method coupled with the ff relation. Following Kniazev et al. (2004), we have also determined $(O/H)_{7325}$ abundances, based on the intensities of the [OII] $\lambda\lambda 7320, 7330$ auroral lines, and using a small modification of the classic T_e method. Both $(O/H)_{ff}$ and $(O/H)_{7325}$ abundances have been derived with one- and two-dimensional $t_2 - t_3$ relations.

It was found that reliable $(\text{O}/\text{H})_{\text{ff}}$ abundances can be derived with measurements of only $[\text{OIII}]\lambda 4959 + \lambda 5007$ and $[\text{OIII}]\lambda 4363$ line intensities. The parametric two-dimensional $t_2 - t_3$ relation appears to provide more accurate values of t_2 as compared to the one-dimensional relation. We show that the differences between $(\text{O}/\text{H})_{\text{ff}}$ and $(\text{O}/\text{H})_{7325}$ abundances for our sample of H II regions are caused more by measurement uncertainties of the $[\text{OIII}]\lambda 4363$ line intensity than by those of the $[\text{OII}]\lambda 7320 + \lambda 7330$ line intensity.

Our final list contains 29 galaxies, with 84 separate determinations of H II region oxygen abundance. Because of our selection methods, the metallicity of our galaxies lies in the narrow range $8.2 \lesssim 12 + \log (\text{O}/\text{H}) \lesssim 8.4$. The radial distribution of oxygen abundances in the disk of the spiral galaxy NGC 4490 is determined for the first time. The objects in our sample generally follow the luminosity – metallicity relation established for galaxies. An exception is NGC 4490 which has an oxygen abundance lower than that of other galaxies of similar luminosities.

T.X.T. and L.S.P. acknowledge the support of National Science Foundation grant AST02-05785. L.S.P. thanks the hospitality of the Astronomy Department of the University of Virginia where this investigation was carried out. We thank the referee for the recommendations which improve the clarity of the presentation. We thank Yuri Izotov for useful discussions. This research has made use of the NASA/IPAC Extragalactic Database (NED) which is operated by the Jet Propulsion Laboratory, California Institute of Technology, under contract with the National Aeronautic and Space Administration. We acknowledge the work of the SDSS team. Funding for the SDSS has been provided by the Alfred P. Sloan Foundation, the Participating Institutions, the National Aeronautics and Space Administration, the National Science Foundation, the U.S. Department of Energy, the Japanese Monbukagakusho, and the Max Planck Society.

REFERENCES

- Aller, L.H. 1984, *Physics of thermal gaseous nebulae*, D. Reidel Publishing Company, Dordrecht.
- Bresolin, F. 2007, *ApJ*, 656, 186
- Campbell, A., Terlevich, R., & Melnick, J. 1986, *MNRAS*, 223, 811
- Deharveng, L., Peña, M., Caplan, J., & Costero, R. 2000, *MNRAS*, 311, 329
- Devost, D., Roy, J.-R., & Drissen, L. 1997, *AJ*, 482, 765

- de Vaucouleurs, G., de Vaucouleurs, A., Corvin, H.G., Buta, R.J., Paturel, J., & Fouque, P. Third Reference Catalog of bright Galaxies., 1991. – New York: Springer
- Dopita, M.A., & Evans, I.N. 1986, *ApJ*, 307, 431
- Edmunds, M.G., & Pagel, B.E.J. 1984, *MNRAS*, 211, 507
- Izotov, Y.I., Stasińska, G., Guseva, N.G., & Thuan, T.X. 2004, *A&A*, 415, 87
- Izotov, Y.I., Stasińska, G., Meynet, G., Guseva, N.G., & Thuan, T.X. 2006, *A&A*, 448, 955
- Izotov, Y.I., Thuan, T.X., & Lipovetsky, V.A. 1994, *ApJ*, 435, 647
- Izotov, Y.I., Thuan, T.X., & Lipovetsky, V.A. 1997, *ApJS*, 108, 1
- Garnett, D.R. 1992, *AJ*, 103, 1330
- Garnett, D.R., & Kennicutt, R.C. 1994, *ApJ*, 426, 123
- Garnett, D.R., Shields, G.A., Peimbert, M., Torres-Peimbert, S., Skillman, E.D., Dufour, R.J., Terlevich, E., & Terlevich, R.J. 1999, *ApJ*, 513, 168
- Hodge, P.W., Gurwell, M., Goldader, J.D., & Kennicutt, R.C. 1990, *ApJS*, 73, 661
- Kennicutt, R.C., Bresolin, F., & Garnett, D.R. 2003, *ApJ*, 591, 801
- Kennicutt, R.C., & Garnett, D.R. 1996, *ApJ*, 456, 504
- Kinkel, U., & Rosa, M.R. 1994, *A&A*, 282, L37
- Kniazev, A.Y., Grebel, E.K., Hao, L., Strauss, M., Brinkmann, J., & Fukugita, M. 2003, *ApJ*, 593, L73
- Kniazev, A.Y., Pustilnik, S.A., Grebel, E.K., Lee, H., & Pramskij, A.G. 2004, *ApJSS*, 153, 429
- Luridiana, V., Esteban, C., Peimbert, M., & Peimbert, A. 2002, *Rev. Mex. AA*, 36, 97
- McCall, M.L., Rybski, P.M., & Shields, G.A. 1985, *ApJS*, 57, 1
- McGaugh, S.S. 1991, *ApJ*, 380, 140
- Oey, M.S., & Shields, J.C. 2000, *ApJ*, 539, 687
- Pagel, B.E.J., Edmunds, M.G., Fosbury, R.A.E., & Webster, B.L. 1978, *MNRAS*, 184, 569

- Pagel, B.E.J., Edmunds, M.G., Blackwell, D.E., Chun, M.S., & Smith, G. 1979, MNRAS, 189, 95
- Pagel, B.E.J., Simonson, E.A., Terlevich, R.J., & Edmunds M.G. 1992, MNRAS, 255, 325
- Pilyugin, L.S. 2000, A&A, 362, 325
- Pilyugin, L.S. 2001a, A&A, 369, 594
- Pilyugin, L.S. 2001b, A&A, 373, 56
- Pilyugin, L.S. 2005, A&A, 436, 1L
- Pilyugin, L.S. 2007, MNRAS, 375, 685
- Pilyugin, L.S., & Thuan, T.X. 2005, ApJ, 631, 231
- Pilyugin, L.S., Thuan, T.X., & Vílchez J.M. 2006a, MNRAS, 367, 1139
- Pilyugin, L.S., Vílchez, J.M., & Thuan, T.X. 2006b, MNRAS, 370, 1928
- Pilyugin, L.S., Thuan, T.X., & Vílchez, J.M. 2007, MNRAS, 376, 353
- Pilyugin, L.S., Vílchez, J.M., & Contini, T., 2004, A&A, 425, 849
- Rayo, J.F., Peimbert, M., & Torres-Peimbert, S. 1982, ApJ, 255, 1
- Shields, G.A., & Searle, L. 1978, ApJ, 222, 821
- Smith, H.E. 1975, ApJ, 199, 591
- Torres-Peimbert, S., Peimbert, M., & Fierro J. 1989, ApJ, 345, 186
- York, D.G., Adelman, J., Anderson, J.E., Jr., et al. 2000, AJ, 120, 1579
- van Zee, L., Salzer, J.J., Haynes, M.P., O'Donoghue, A.A., & Balonek T.J. 1998, AJ, 116, 2805

Table 1. Nearby galaxy sample

galaxy name ^a	coordinates	morphological type	morphological type code	apparent B magnitude	redshift	absolute B magnitude	other names
M101	14 ^h 03 ^m 12.44 ^s + 54°20′53.0″	SABc	5.9±0.3	8.39	0.000804	-20.84	M102, NGC5457, UGC08981, ARP026, VV344, VV456, PGC050063
NGC428	01 ^h 12 ^m 55.74 ^s + 00°58′53.3″	SABm	8.6±1.0	11.94	0.003843	-19.48	UGC00763, UM309 PGC004367
NGC450	01 ^h 15 ^m 30.55 ^s - 00°51′39.2″	SABc	5.9±0.5	12.72	0.005874	-19.69	UGC00806, PGC004540
NGC1110	02 ^h 49 ^m 09.37 ^s - 07°50′19.5″	SBm	8.8±1.0	14.58	0.004446	-18.17	UGCA043, PGC010673
NGC2541	08 ^h 14 ^m 40.06 ^s + 49°03′41.7″	SABc	6.0±0.4	12.18	0.001828	-18.67	UGC04284, PGC023110
NGC2552	08 ^h 19 ^m 19.54 ^s + 50°00′28.5″	SABm	9.0±0.5	12.68	0.001748	-17.97	UGC04325, PGC023340
NGC3023	09 ^h 49 ^m 52.70 ^s + 00°37′04.1″	SABc	5.4±0.8	13.39	0.006268	-19.47	UGC05269, VV620, PGC028272
NGC3319	10 ^h 39 ^m 09.51 ^s + 41°41′13.0″	SBc	5.9±0.4	11.72	0.002465	-19.43	UGC05789, PGC031671
NGC3432	10 ^h 52 ^m 30.93 ^s + 36°37′09.3″	SBm	8.9±0.5	11.64	0.002055	-19.81	UGC05986, ARP206, PGC032643, VV011
NGC3991	11 ^h 57 ^m 30.48 ^s + 32°20′00.3″	IB	9.7±1.3	13.52	0.010647	-20.99	UGC06933, PGC037613, VV523, CG0137
NGC3995	11 ^h 57 ^m 44.15 ^s + 32°17′39.7″	SABm	8.8±0.8	12.73	0.010854	-21.55	UGC06944, PGC037624, VV249, ARP313, CG0139
NGC4490	12 ^h 30 ^m 36.37 ^s + 41°38′37.2″	SBcd	7.0±0.2	9.77	0.001885	-21.52	UGC07651, ARP269, PGC041333, VV030
NGC5669	14 ^h 32 ^m 43.92 ^s + 09°53′28.2″	SABc	6.0±0.4	12.66	0.004547	-19.41	UGC09353, PGC051973
IC2828	11 ^h 27 ^m 11.03 ^s + 08°43′53.1″			14.70	0.003466	-16.49	PGC035225, Tol1124+090
UGC05189	09 ^h 42 ^m 56.75 ^s + 09°28′18.3″	I	9.9±0.5	14.62	0.010720	-19.34	PGC027784, VV547
UGC05249	09 ^h 47 ^m 45.37 ^s + 02°37′38.6″	Scd	6.8±0.8	14.50	0.006252	-18.95	PGC028148
UGC06596	11 ^h 37 ^m 51.06 ^s + 56°08′32.7″	IB	9.9±0.5	17.12	0.007609	-16.28	PGC036000, VV148
UGC09979	15 ^h 42 ^m 19.34 ^s + 00°28′31.0″	IB	9.8±1.0	14.93	0.006541	-18.56	PGC055833, DDO201
UGCA154	09 ^h 16 ^m 45.52 ^s + 53°26′34.0″	S?	3.2±5.0	14.71	0.007456	-18.48	PGC026188, MRK0104, SBS0913+536
UGCA322	13 ^h 04 ^m 31.19 ^s - 03°34′20.6″	Sd	7.6±1.0	14.51	0.004536	-17.31	PGC045195
PGC001586	00 ^h 25 ^m 19.93 ^s + 00°31′31.1″	S?	4.6±5.0	16.61	0.014045	-17.68	HS0022+0014, UM241
PGC023706	08 ^h 27 ^m 18.05 ^s + 46°02′02.8″	S?	3.9±5.0	15.80	0.007344	-17.25	
PGC051971	14 ^h 32 ^m 45.11 ^s + 02°54′54.2″	Sbc	4.2±0.8	15.12	0.005070	-17.02	Tol1430+031
PGC056006	15 ^h 46 ^m 30.73 ^s + 45°59′53.9″			14.88	0.008878	-18.28	MRK0490
HS1103+4346	11 ^h 06 ^m 29.03 ^s + 43°30′41.3″	BCG			0.021401		CG1377

Table 1—Continued

galaxy name ^a	coordinates	morphological type	morphological type code	apparent B magnitude	redshift	absolute B magnitude	other names
HS1132+4416	$11^h 34^m 53.68^s + 44^\circ 00' 16.4''$	BCG			0.018481		
UM330	$01^h 30^m 03.62^s + 00^\circ 44' 34.9''$				0.017000		
CG1419	$11^h 23^m 17.23^s + 41^\circ 03' 37.2''$				0.010529		
SDSS125446.33+153529.8	$12^h 54^m 46.32^s + 15^\circ 35' 29.9''$				0.008792		

^aThe galaxies are listed in order of name category, with the following categories in descending order:

M – Messier catalogue of nebulae,
 NGC – New General Catalogue,
 IC – Index Catalogue,
 UGC – Uppsala General Catalog of Galaxies,
 UGCA – Uppsala General Catalog Appendix,
 PGC – Principal Galaxy Catalog,
 HS – Hamburg/ESO QSO Survey,
 UM – University of Michigan Emission Line Objects,
 CG - Compact Group,
 SDSS - Sloan Digital Sky Survey.

Table 2. Line intensities and derived oxygen abundances of H II regions in galaxies of nearby sample

galaxy name	spectrum number	R_G^a	$[\text{OIII}]^b$ $\lambda 4363$	$[\text{OIII}]^b$ $\lambda, \lambda 4959, 5007$	$[\text{OII}]^b$ $\lambda 7325$	t_3^c	$(\text{O}/\text{H})_{7325}^d$	$(\text{O}/\text{H})_{ff}^d$	$(\text{O}/\text{H})_{7325}^e$	$(\text{O}/\text{H})_{ff}^e$
M101	1325 52762 345	0.20	0.0045± 0.0032	1.40± 0.01	0.031± 0.004	0.90	8.41	8.55	8.28	8.45
M101	1325 52762 356	0.32	0.0072± 0.0052	1.74± 0.01	0.033± 0.003	0.96	8.36	8.54	8.20	8.41
M101	1323 52797 011	0.33	0.0038± 0.0033	2.30± 0.02	0.039± 0.005	0.76	8.59	8.45	8.75	8.53
M101	1325 52762 348	0.34	0.0178± 0.0052	3.79± 0.02	0.026± 0.004	1.00	8.23	8.32	8.24	8.33
M101	1324 53088 236	0.41	0.0272± 0.0188	2.96± 0.04	0.000± 0.000	1.24	...	8.52	...	8.26
M101	1325 52762 352	0.43	0.0220± 0.0031	5.52± 0.07	0.060± 0.005	0.95	8.46	8.35	8.58	8.39
M101	1323 52797 009	0.43	0.0126± 0.0070	3.34± 0.04	0.038± 0.012	0.94	8.36	8.34	8.40	8.37
M101	1323 52797 013	0.44	0.0097± 0.0025	2.30± 0.03	0.042± 0.010	0.96	8.39	8.45	8.30	8.38
M101	1323 52797 002	0.46	0.0196± 0.0028	5.16± 0.07	0.059± 0.004	0.94	8.47	8.35	8.59	8.40
M101	1324 53088 221	0.47	0.0177± 0.0053	5.03± 0.03	0.040± 0.012	0.92	8.43	8.37	8.54	8.42
M101	1323 52797 001	0.50	0.0073± 0.0079	2.51± 0.03	0.065± 0.012	0.87	8.59	8.40	8.65	8.43
M101	1324 53088 223	0.54	0.0566± 0.0069	7.65± 0.35	0.034± 0.015	1.15	8.23	8.23	8.25	8.25
M101	1323 52797 008	0.54	0.0135± 0.0027	4.11± 0.03	0.052± 0.004	0.90	8.47	8.36	8.59	8.41
M101	1324 53088 271	0.54	0.0138± 0.0043	2.94± 0.03	0.051± 0.004	1.00	8.39	8.38	8.34	8.34
M101	1324 53088 279	0.55	0.0352± 0.0038	5.01± 0.04	0.045± 0.005	1.13	8.22	8.25	8.20	8.23
M101	1324 53088 263	0.58	0.0587± 0.0041	6.96± 0.07	0.038± 0.005	1.21	8.17	8.19	8.17	8.19
M101	1325 52762 350	0.67	0.0386± 0.0033	6.18± 0.30	0.035± 0.004	1.09	8.25	8.25	8.27	8.27
M101	1323 52797 016	0.67	0.0343± 0.0071	4.83± 0.06	0.040± 0.008	1.14	8.20	8.26	8.16	8.23
M101	1324 53088 234	0.81	0.0686± 0.0032	6.31± 0.04	0.051± 0.003	1.33	8.04	...
M101	1323 52797 066	1.05	0.0625± 0.0120	4.91± 0.06	0.054± 0.024	1.42	7.89	...
NGC428	695 52202 325	0.42	0.0371± 0.0088	4.33± 0.19	0.056± 0.008	1.21	8.23	8.31	8.10	8.21
NGC428	1499 53001 453	0.43	0.0145± 0.0080	4.25± 0.02	0.039± 0.006	0.91	8.41	8.35	8.51	8.40
NGC428	1499 53001 458	0.47	0.0230± 0.0047	4.45± 0.09	0.057± 0.004	1.03	8.36	8.29	8.39	8.30
NGC428	695 52202 324	0.51	0.0275± 0.0118	3.96± 0.02	0.045± 0.019	1.13	8.23	8.32	8.15	8.25
NGC428	694 52209 602	0.53	0.0269± 0.0047	6.41± 0.12	0.029± 0.006	0.96	8.39	8.37	8.46	8.40
NGC450	695 52202 137	0.56	0.0251± 0.0024	5.60± 0.04	0.038± 0.003	0.98	8.36	8.32	8.43	8.36
NGC450	398 51789 294	0.66	0.0170± 0.0058	3.96± 0.03	0.037± 0.005	0.97	8.32	8.32	8.36	8.34
NGC1110	457 51901 304	0.10	0.0475± 0.0124	5.65± 0.05	0.040± 0.008	1.21	8.15	8.22	8.12	8.19
NGC1110	457 51901 309	0.76	0.0718± 0.0038	7.80± 0.04	0.040± 0.004	1.25	8.16	8.18	8.16	8.18

Table 2—Continued

galaxy name	spectrum number	R_G^a	[OIII] ^b $\lambda 4363$	[OIII] ^b $\lambda, \lambda 4959, 5007$	[OII] ^b $\lambda 7325$	t_3^c	(O/H) ₇₃₂₅ ^d	(O/H) _{ff} ^d	(O/H) ₇₃₂₅ ^e	(O/H) _{ff} ^e
NGC2541	440 51885 151	0.41	0.0302± 0.0030	5.89± 0.03	0.036± 0.004	1.02	8.31	8.29	8.37	8.32
NGC2541	440 51912 136	0.41	0.0277± 0.0046	5.92± 0.09	0.029± 0.049	0.99	8.33	8.32	8.38	8.35
NGC2552	440 51885 608	0.08	0.0149± 0.0054	3.94± 0.08	0.038± 0.008	0.94	8.37	8.33	8.44	8.37
NGC2552	440 51912 627	0.08	0.0230± 0.0085	3.57± 0.03	0.048± 0.011	1.10	8.28	8.35	8.18	8.28
NGC3023	267 51608 384	0.41	0.0384± 0.0041	5.49± 0.03	0.035± 0.004	1.13	8.19	8.24	8.18	8.23
NGC3023	481 51908 289	0.46	0.0715± 0.0036	9.12± 0.37	0.030± 0.002	1.18	8.25	8.24	8.27	8.26
NGC3319	1361 53047 222	0.72	0.0373± 0.0055	6.04± 0.03	0.038± 0.005	1.08	8.26	8.25	8.29	8.27
NGC3319	1360 53033 634	0.75	0.0352± 0.0037	6.63± 0.32	0.034± 0.003	1.03	8.32	8.30	8.38	8.33
NGC3319	1361 53047 221	0.81	0.0344± 0.0031	5.80± 0.17	0.050± 0.003	1.07	8.31	8.26	8.35	8.28
NGC3432	2007 53474 221	0.01	0.0076± 0.0073	2.05± 0.03	0.029± 0.007	0.93	8.33	8.46	8.26	8.41
NGC3432	2090 53463 550	0.14	0.0426± 0.0033	6.27± 0.23	0.033± 0.003	1.12	8.21	8.23	8.23	8.25
NGC3432	2090 53463 545	0.19	0.0138± 0.0059	2.87± 0.02	0.000± 0.000	1.00	...	8.39	...	8.34
NGC3991	2095 53474 352	0.82	0.0158± 0.0086	3.03± 0.02	0.045± 0.005	1.03	8.33	8.38	8.25	8.32
NGC3991	1991 53446 584	1.07	0.0165± 0.0033	4.04± 0.02	0.040± 0.003	0.96	8.35	8.32	8.41	8.36
NGC3995	1991 53446 587	0.26	0.0270± 0.0136	3.59± 0.03	0.038± 0.012	1.16	8.18	8.38	8.05	8.25
NGC3995	1991 53446 588	0.67	0.0278± 0.0134	3.45± 0.02	0.060± 0.011	1.19	8.31	8.41	8.10	8.25
NGC4490	1452 53112 009	0.12	0.0166± 0.0031	4.24± 0.04	0.045± 0.003	0.94	8.39	8.33	8.47	8.37
NGC4490	1454 53090 299	0.14	0.0227± 0.0036	5.50± 0.06	0.047± 0.003	0.96	8.42	8.34	8.51	8.38
NGC4490	1984 53433 366	0.16	0.0163± 0.0037	4.03± 0.02	0.039± 0.003	0.95	8.35	8.32	8.41	8.36
NGC4490	1452 53112 016	0.23	0.0248± 0.0038	4.90± 0.04	0.039± 0.003	1.02	8.30	8.28	8.34	8.31
NGC4490	1452 53112 008	0.45	0.0180± 0.0038	4.16± 0.02	0.041± 0.003	0.97	8.34	8.31	8.39	8.34
NGC5669	1709 53533 215	0.81	0.0350± 0.0026	7.04± 0.08	0.052± 0.004	1.01	8.41	8.33	8.49	8.36
NGC5669	1709 53533 216	1.22	0.0230± 0.0144	3.75± 0.03	0.040± 0.012	1.08	8.24	8.33	8.18	8.28
IC2828	1223 52781 128	0.06	0.0239± 0.0105	4.63± 0.05	0.050± 0.006	1.03	8.33	8.28	8.36	8.30
IC2828	1618 52116 413	0.39	0.0587± 0.0151	5.74± 0.05	0.061± 0.024	1.30	8.18	8.22	8.08	8.14

Table 2—Continued

galaxy name	spectrum number	R_G^a	[OIII] ^b $\lambda 4363$	[OIII] ^b $\lambda, \lambda 4959, 5007$	[OII] ^b $\lambda 7325$	t_3^c	(O/H) ₇₃₂₅ ^d	(O/H) _{ff} ^d	(O/H) ₇₃₂₅ ^e	(O/H) _{ff} ^e
UGC05189	1305 52757 274	0.89	0.0280± 0.0074	4.66± 0.04	0.050± 0.006	1.07	8.29	8.27	8.28	8.27
UGC05189	1305 52757 269	1.04	0.0518± 0.0026	7.25± 0.31	0.045± 0.003	1.14	8.26	8.23	8.29	8.25
UGC05249	481 51908 335	0.03	0.0172± 0.0096	3.16± 0.03	0.039± 0.010	1.04	8.28	8.37	8.20	8.31
UGC05249	480 51989 578	0.03	0.0109± 0.0031	3.22± 0.04	0.043± 0.005	0.91	8.42	8.36	8.48	8.39
UGC06596	1309 52762 012	0.09	0.0344± 0.0092	5.04± 0.03	0.047± 0.015	1.12	8.24	8.25	8.22	8.24
UGC06596	1311 52765 293	0.09	0.0262± 0.0084	5.06± 0.04	0.042± 0.010	1.03	8.31	8.28	8.35	8.31
UGC09979	315 51663 594	0.27	0.0314± 0.0178	3.65± 0.12	0.069± 0.022	1.21	8.33	8.40	8.11	8.23
UGC09979	342 51691 352	0.27	0.0323± 0.0121	4.01± 0.03	0.054± 0.011	1.19	8.25	8.34	8.11	8.23
UGCA154	553 51999 596	0.05	0.0335± 0.0089	5.51± 0.03	0.038± 0.007	1.08	8.25	8.25	8.27	8.27
UGCA154	554 52000 205	0.41	0.0289± 0.0069	4.56± 0.04	0.043± 0.005	1.09	8.24	8.27	8.22	8.26
UGCA322	339 51692 089	0.58	0.0461± 0.0112	4.86± 0.04	0.053± 0.011	1.26	8.18	8.28	8.05	8.17
UGCA322	339 51692 083	0.60	0.0341± 0.0043	6.04± 0.06	0.040± 0.003	1.05	8.30	8.27	8.35	8.30
PGC01586	390 51816 581	0.02	0.0370± 0.0118	4.51± 0.02	0.052± 0.010	1.20	8.22	8.29	8.12	8.21
PGC01586	390 51900 596	0.02	0.0203± 0.0057	4.34± 0.05	0.053± 0.009	0.99	8.37	8.30	8.42	8.33
PGC23706	548 51986 517	0.02	0.0309± 0.0064	4.50± 0.02	0.056± 0.006	1.12	8.28	8.28	8.23	8.24
PGC23706	549 51981 281	0.45	0.0439± 0.0131	4.59± 0.05	0.056± 0.010	1.26	8.20	8.31	8.05	8.18
PGC51971	535 51999 563	0.03	0.0212± 0.0180	3.37± 0.04	0.058± 0.015	1.09	8.35	8.37	8.23	8.29
PGC51971	585 52027 049	0.37	0.0300± 0.0117	4.38± 0.03	0.068± 0.013	1.12	8.33	8.29	8.27	8.25
PGC56006	1333 52782 613	0.01	0.0211± 0.0081	3.81± 0.02	0.051± 0.007	1.05	8.32	8.32	8.29	8.29
PGC56006	1168 52731 256	0.39	0.0242± 0.0091	3.99± 0.03	0.037± 0.007	1.08	8.22	8.31	8.19	8.27
HS1103+4346	1363 53053 138	0.02	0.0556± 0.0067	6.94± 0.02	0.043± 0.006	1.18	8.20	8.20	8.21	8.21
HS1103+4346	1364 53061 295	0.51	0.0705± 0.0053	8.14± 0.07	0.043± 0.004	1.22	8.21	8.20	8.22	8.20

Table 2—Continued

galaxy name	spectrum number	R_G^a	$[\text{OIII}]^b$ $\lambda 4363$	$[\text{OIII}]^b$ $\lambda, \lambda 4959, 5007$	$[\text{OII}]^b$ $\lambda 7325$	t_3^c	$(\text{O}/\text{H})_{7325}^d$	$(\text{O}/\text{H})_{ff}^d$	$(\text{O}/\text{H})_{7325}^e$	$(\text{O}/\text{H})_{ff}^e$
HS1132+4416	1367 53083 292	0.01	0.0203 ± 0.0102	4.77 ± 0.03	0.043 ± 0.010	0.97	8.37	8.32	8.44	8.36
HS1132+4416	1366 53063 083	0.51	0.0407 ± 0.0042	6.53 ± 0.02	0.037 ± 0.003	1.09	8.27	8.26	8.30	8.28
UM330	1079 52621 616	0.09	0.0292 ± 0.0107	3.83 ± 0.04	0.040 ± 0.023	1.16	8.19	8.35	8.07	8.24
UM330	1078 52643 353	0.21	0.0289 ± 0.0098	5.39 ± 0.06	0.067 ± 0.014	1.04	8.38	8.28	8.44	8.30
CG1419	1440 53084 103	0.03	0.0368 ± 0.0063	5.99 ± 0.03	0.041 ± 0.006	1.08	8.27	8.25	8.30	8.27
CG1419	1996 53436 330	0.03	0.0458 ± 0.0081	6.05 ± 0.04	0.046 ± 0.008	1.16	8.21	8.22	8.21	8.22
SDSS125446.33+153529.8	1771 53498 335	0.01	0.0513 ± 0.0168	6.50 ± 0.06	0.050 ± 0.021	1.18	8.22	8.21	8.22	8.21
SDSS125446.33+153529.8	1770 53171 612	0.01	0.0468 ± 0.0169	5.93 ± 0.06	0.045 ± 0.014	1.18	8.19	8.22	8.18	8.20

^aGalactocentric distance of the H II region normalized to the R_{25} isophotal radius

^bDereddened line intensity and its uncertainty on a scale where $I(H\beta) = 1$

^cElectron temperature within the [O III] zone in units of 10^4K

^d t_2 abundances calculated with Eq. (16) and given as $12 + \log (\text{O}/\text{H})$

^e t_2 abundances calculated with Eq. (15) and given as $12 + \log (\text{O}/\text{H})$

Table 3. Comparison of $(\text{O}/\text{H})_{7325}$ abundances with those of other authors

galaxy name	spectrum number	$(\text{O}/\text{H})_{7325}^{\text{a}}$ this study	$(\text{O}/\text{H})_{7325}^{\text{a}}$ Izotov et al. (2006)	$(\text{O}/\text{H})_{7325}^{\text{a}}$ Kniazev et al (2004)
M101	1325 52762 348	8.24	8.26	
M101	1325 52762 352	8.58	8.48	
M101	1323 52797 002	8.59	8.51	
M101	1323 52797 008	8.59	8.53	
M101	1325 52762 350	8.27	8.22	
M101	1323 52797 016	8.16	8.07	
NGC450	398 51789 294	8.36	8.40	8.18
NGC1110	457 51901 304	8.12	8.13	8.06
NGC1110	457 51901 309	8.16	8.03	8.03
NGC2541	440 51885 151	8.37	8.30	8.23
NGC2552	440 51885 608	8.44	8.39	8.28
NGC3023	267 51608 384	8.18	7.99	8.10
NGC3023	481 51908 289	8.27	8.12	8.08
IC2828	1223 52781 128	8.36	8.22	
UGC05189	1305 52757 269	8.29	8.24	
UGC05249	481 51908 335	8.20	8.23	
UGCA154	553 51999 596	8.27	8.22	
UGCA154	554 52000 205	8.22		8.15
UGCA322	339 51692 089	8.05		7.96
UGCA322	339 51692 083	8.35	8.15	8.23
PGC001586	390 51900 596	8.42	8.38	8.21
PGC023706	548 51986 517	8.23	8.23	8.05
PGC023706	549 51981 281	8.05	8.16	8.13
PGC051971	535 51999 563	8.23	8.30	
PGC051971	585 52027 049	8.27	8.10	8.18
PGC056006	1333 52782 613	8.29	8.26	

^aOxygen abundances are given as $12 + \log (\text{O}/\text{H})$; they are derived with the one-dimensional $t_2 - t_3$ relation

Table 4. Absolute blue luminosity and central metallicity of galaxies in nearby sample

galaxy name	M_B	central (O/H) ^a t_2 from Eq.(16)	central (O/H) ^a t_2 from Eq.(15)
NGC1110	-18.17	8.19	8.15
NGC2552	-17.97	8.33	8.33
NGC4490	-21.55	8.36	8.43
IC2828	-16.49	8.26	8.24
UGC05249	-18.95	8.36	8.36
UGC06569	-16.28	8.27	8.28
UGCA154	-18.48	8.25	8.26
PGC01586	-17.68	8.30	8.28
PGC23706	-17.25	8.27	8.18
PGC51971	-17.02	8.34	8.26
PGC56006	-18.28	8.29	8.26

^aOxygen abundances are given as $12 + \log (O/H)$

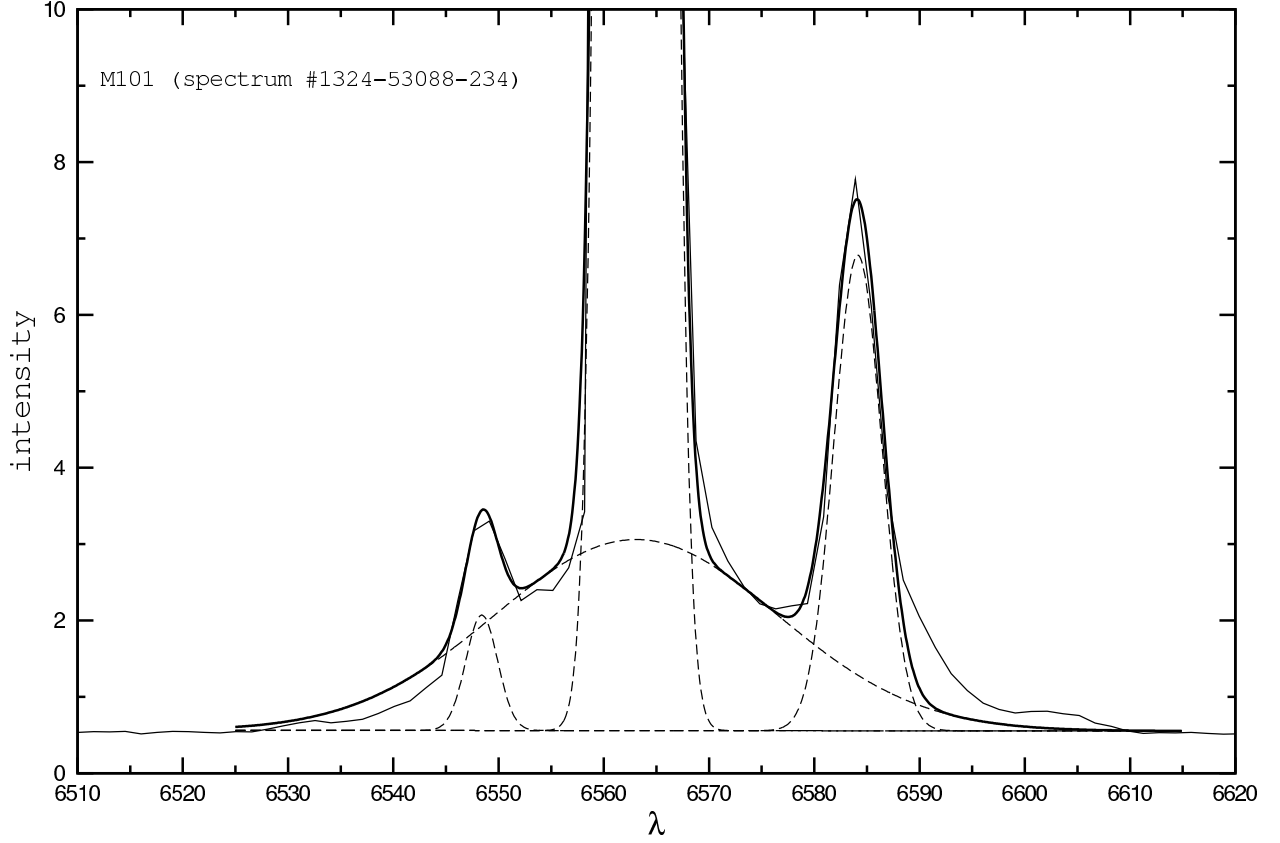


Fig. 1.— Example of a fit to the [NII] λ 6548, H α (both narrow and broad components) and [NII] λ 6584 line profiles. We show here the spectrum # 1324-53088-234 of an H II region in the disk of the spiral galaxy M101. The thin solid line is the observed spectrum, the thick solid line is the fit to it, and the dashed lines are fits to individual lines.

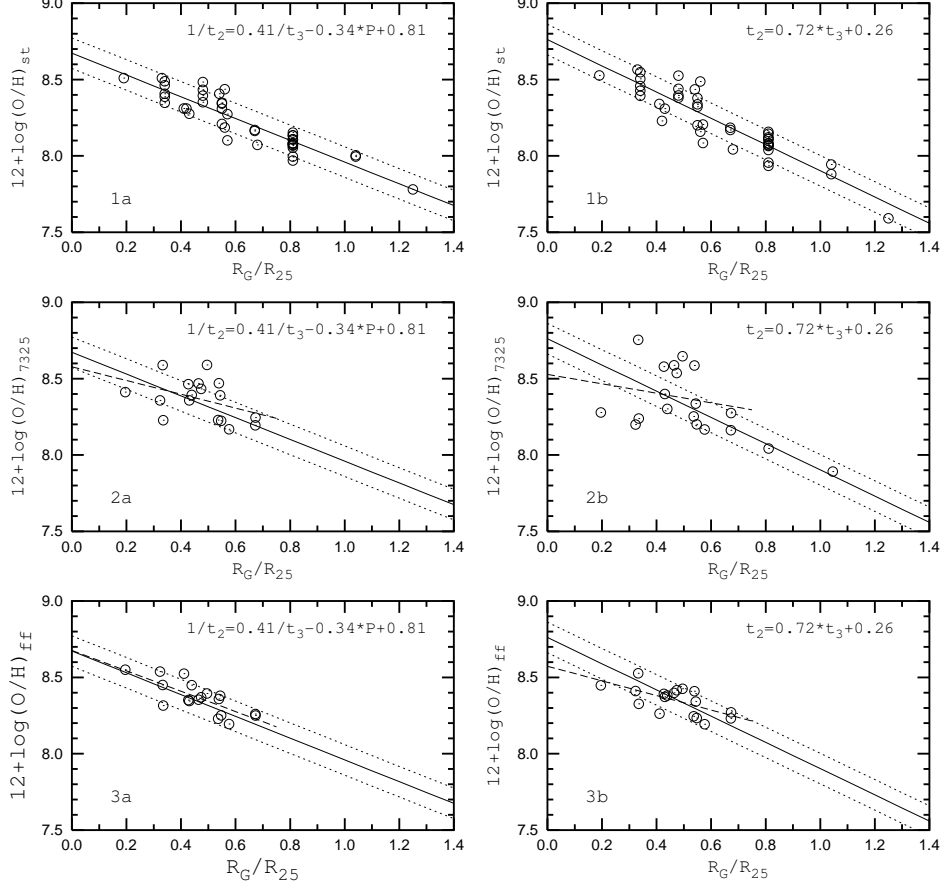


Fig. 2.— Radial distribution of the oxygen abundance in the spiral galaxy M101. The abundances (plotted as open circles) in the left panels have been calculated using the two-dimensional parametric $t_2 - t_3$ relation (Eq. (16)), while those in the right panels have been calculated using the one-dimensional $t_2 - t_3$ relation (Eq. (15)). In all panels, abundances are plotted as a function of galactocentric distance, normalized to the galactic disk isophotal radius R_{25} . *Panels 1a and 1b.* Standard oxygen abundances $(O/H)_{st}$ are plotted. The solid line is the linear least-squares best fit to those abundances. The dotted lines represent shifts of ± 0.1 dex from the best fit. *Panel 2a and 2b.* $(O/H)_{7325}$ abundances are plotted. The dashed line is the linear least-squares best fit to those abundances. The solid and dotted lines in panel 2a are the same as in panel 1a, and those in panel 2b are the same as in panel 1b. *Panel 3a and 3b.* $(O/H)_{ff}$ abundances are plotted. The dashed line is the linear least-squares best fit to those abundances. The solid and dotted lines in panel 3a are the same as in panel 1a, and those in panel 3b are the same as in panel 1b.

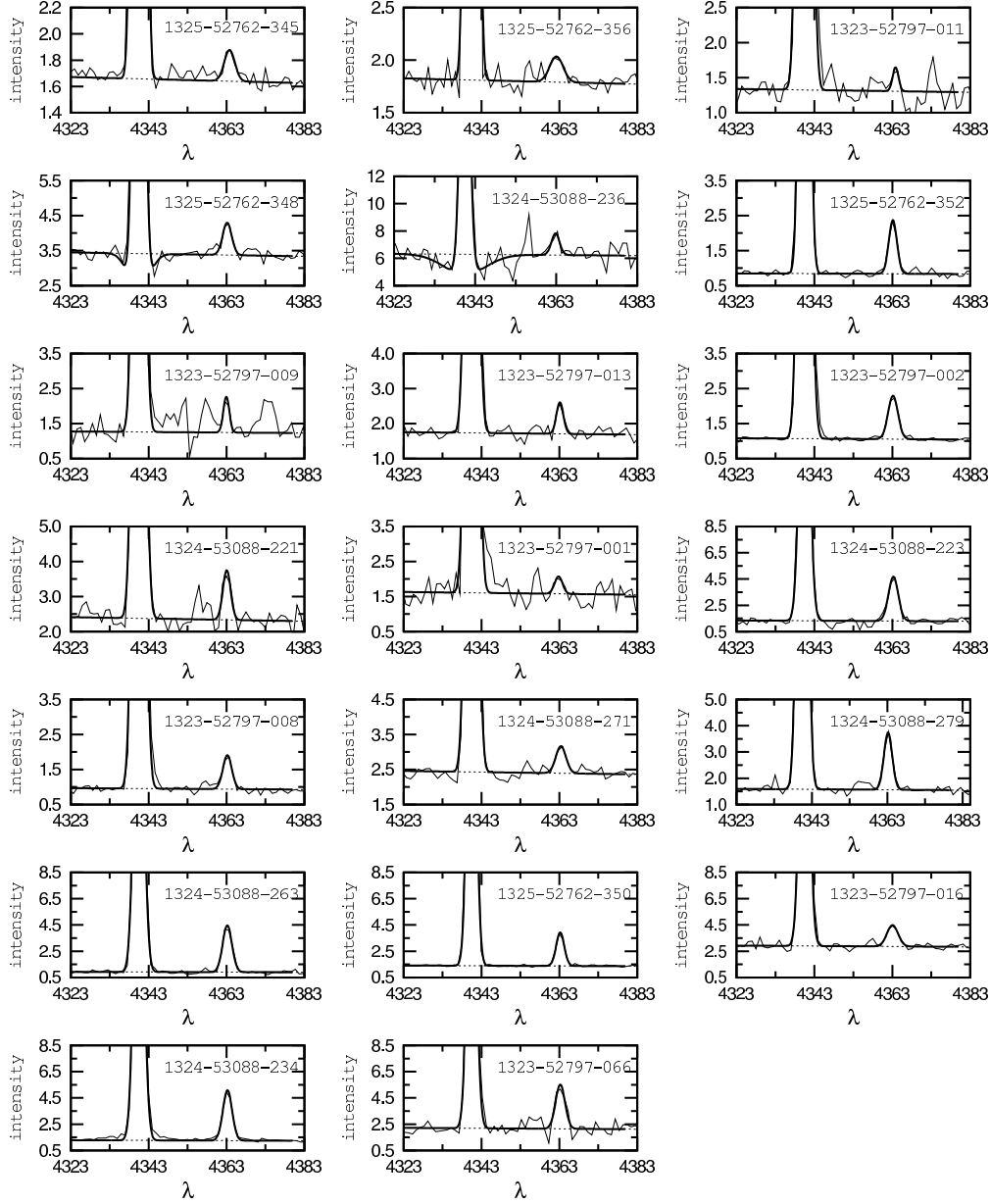


Fig. 3.— Fits to the $H\gamma$ and $[OIII]\lambda 4363$ lines in spectra of H II regions in the spiral galaxy M101. The thin solid line is the observed spectrum, the thick solid line the fit to it, and the dashed line the fit to the continuum.

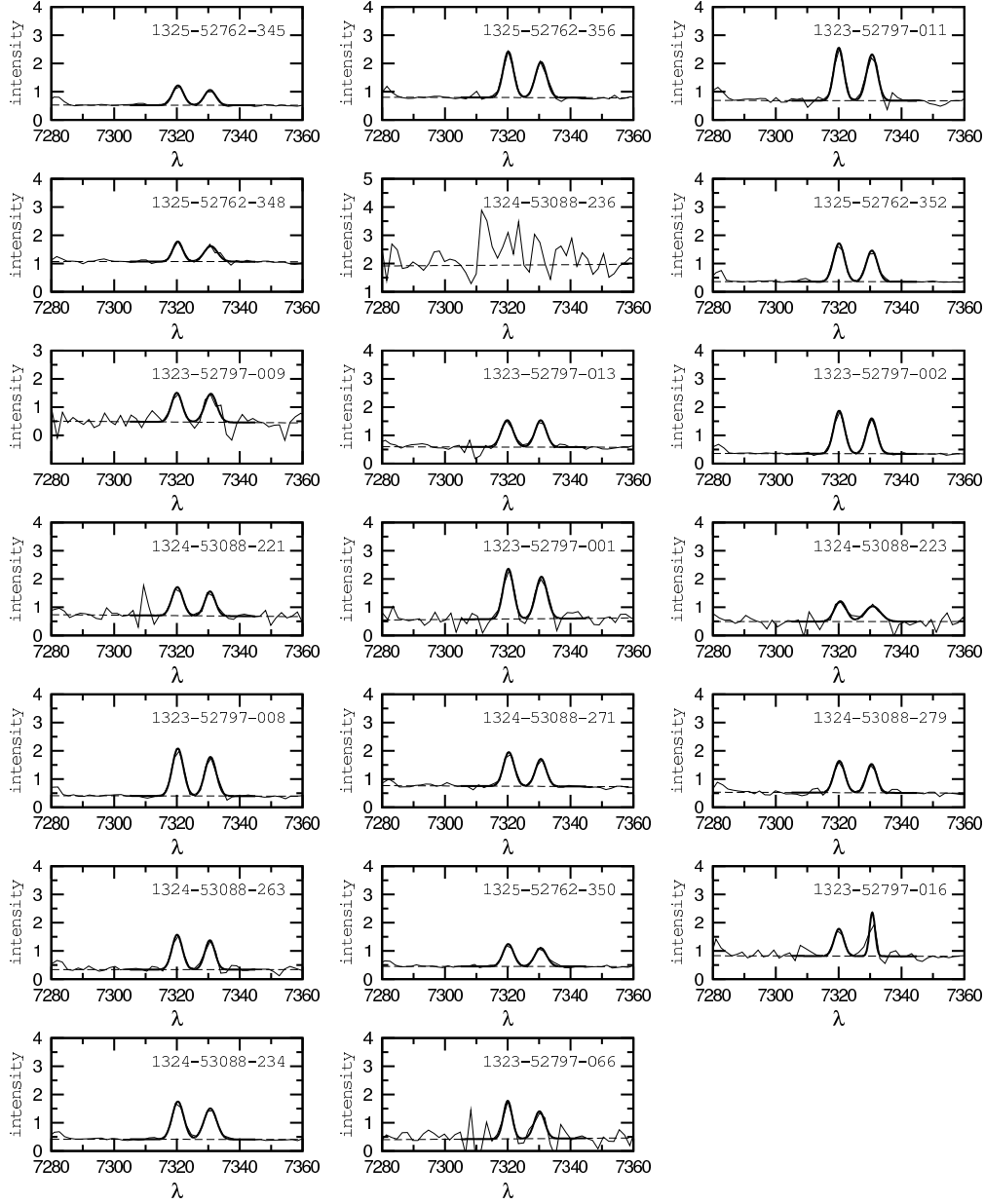


Fig. 4.— Fits to the [OII] λ 7320 and [OII] λ 7330 lines in spectra of H II regions in the spiral galaxy M101. The thin solid line is the observed spectrum, the thick solid line the fit to it, and the dashed line the fit to the continuum.

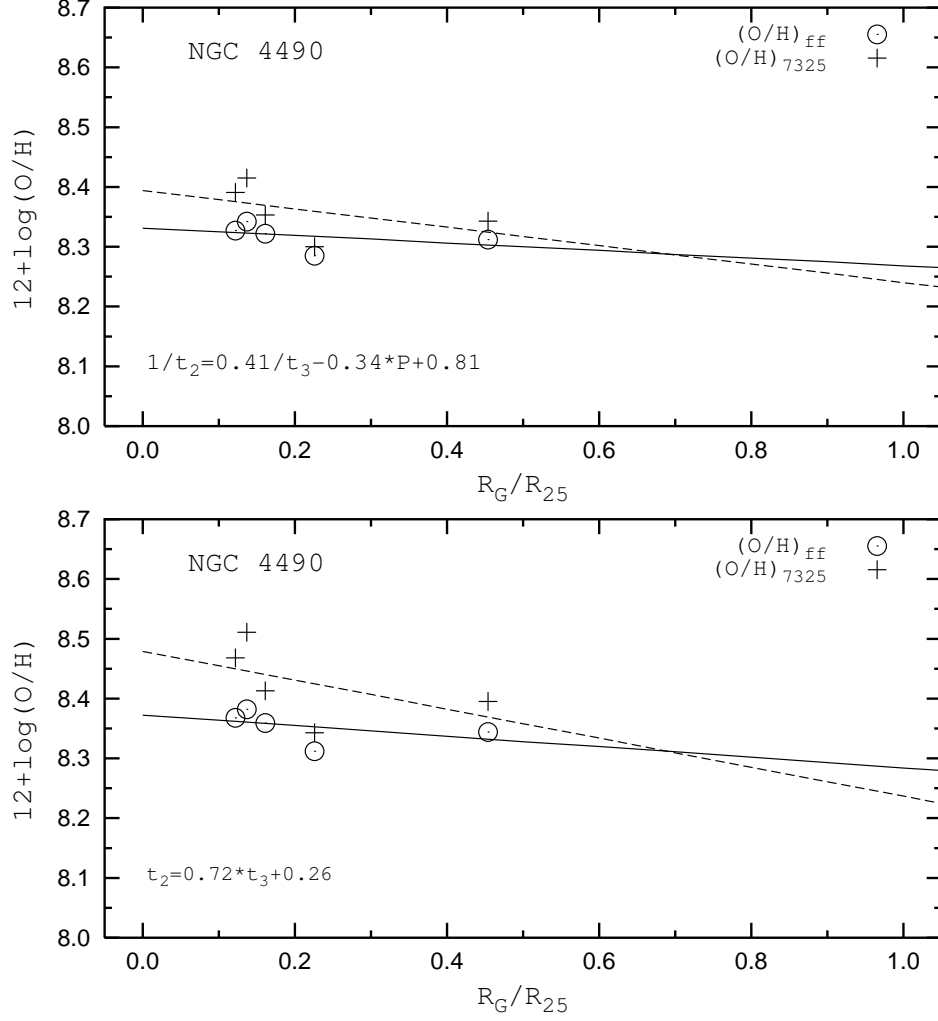


Fig. 5.— Radial distribution of the oxygen abundance in the disk of the spiral galaxy NGC 4490. *Top panel.* $(\text{O}/\text{H})_{\text{ff}}$ (open circles) and $(\text{O}/\text{H})_{7325}$ (plus signs) abundances as a function of galactocentric distance, normalized to the galactic disk isophotal radius R_{25} . The parametric $t_2 - t_3$ relation (Eq. (16)) has been used. The solid line is the linear least-squares fit to $(\text{O}/\text{H})_{\text{ff}}$ data, and the dashed line is the linear least-squares fit to $(\text{O}/\text{H})_{7325}$ data. *Bottom panel.* The same as in the top panel, except that the one-dimensional $t_2 - t_3$ relation (Eq. (15)) has been used.

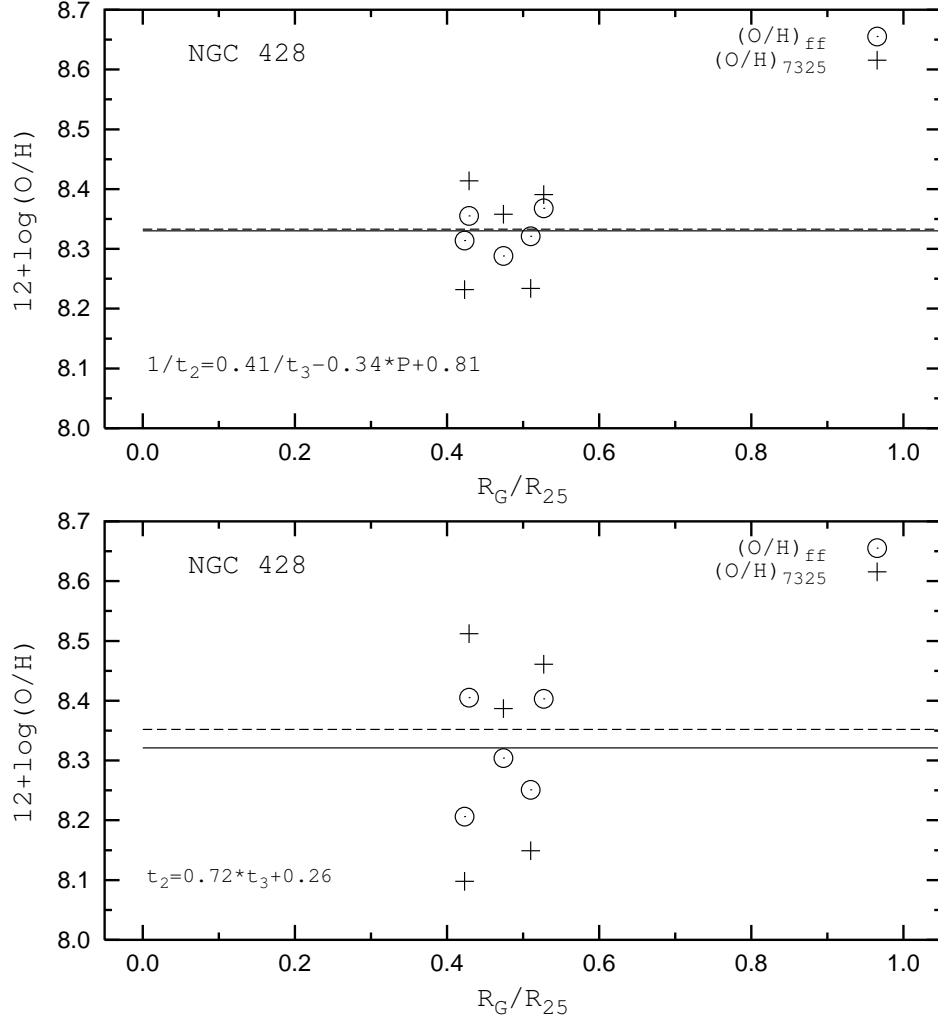


Fig. 6.— Oxygen abundances in the disk of the magellanic irregular galaxy NGC 428. *Top panel.* $(\text{O}/\text{H})_{\text{ff}}$ (open circles) and $(\text{O}/\text{H})_{7325}$ (plus signs) abundances as a function of galactocentric distance, normalized to the galactic disk isophotal radius R_{25} . The parametric $t_2 - t_3$ relation (Eq. (16)) has been used. The solid line shows the mean $(\text{O}/\text{H})_{\text{ff}}$ abundance. The dashed line shows the mean $(\text{O}/\text{H})_{7325}$ abundance. *Bottom panel.* The same as in the top panel, except that the one-dimensional $t_2 - t_3$ relation (Eq. (15)) has been used.

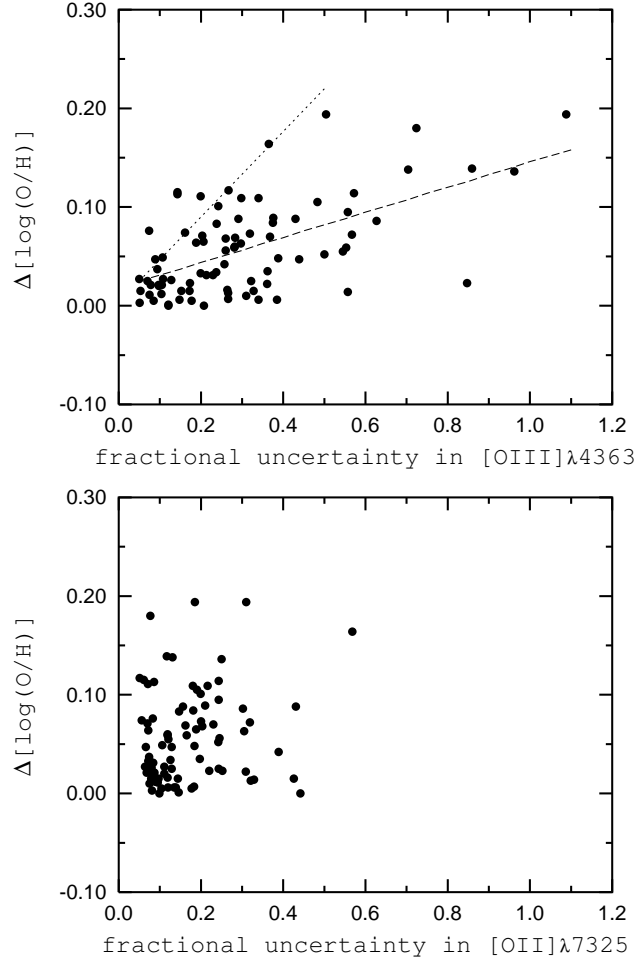


Fig. 7.— *Top panel.* Absolute value of the differences between $\log(\text{O}/\text{H})_{\text{ff}}$ and $\log(\text{O}/\text{H})_{7325}$ abundances ($\Delta\log(\text{O}/\text{H})=|\log(\text{O}/\text{H})_{\text{ff}}-\log(\text{O}/\text{H})_{7325}|$) versus the fractional uncertainty in the [OIII] λ 4363 emission line. Abundances have been determined with the parametric $t_2 - t_3$ relation. The dotted line shows an eye fit to the maximum values of the differences. The dashed line shows the linear least-squares fit to the data. *Bottom panel.* Absolute value of the differences between $\log(\text{O}/\text{H})_{\text{ff}}$ and $\log(\text{O}/\text{H})_{7325}$ abundances versus the fractional uncertainty in the [OII] λ 7320+ λ 7330 emission lines.

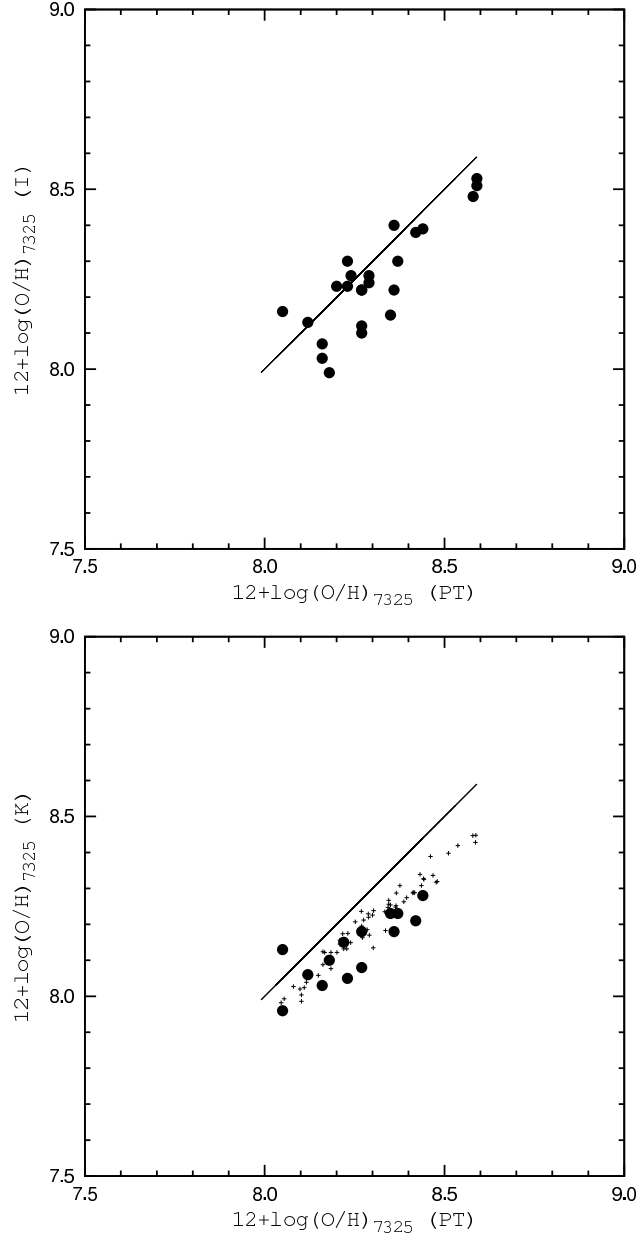


Fig. 8.— Comparison between our $(\text{O}/\text{H})_{7325}$ abundances (labeled PT) derived with the one-dimensional $t_2 - t_3$ relation, and those determined by other authors, based on the same SDSS spectra. *Top panel.* Abundances from Izotov et al. (2006) (labeled I) versus PT abundances (filled circles). The solid line corresponds to equality. *Bottom panel.* Abundances from Kniazev et al. (2004) (labeled K) versus PT abundances (filled circles). The solid line corresponds to equality. The plus signs show $(\text{O}/\text{H})_{7325}$ abundances derived with the $t_2 - t_3$ relation used by Kniazev et al. (2004) as compared to abundances derived with our one-dimensional $t_2 - t_3$ relation.

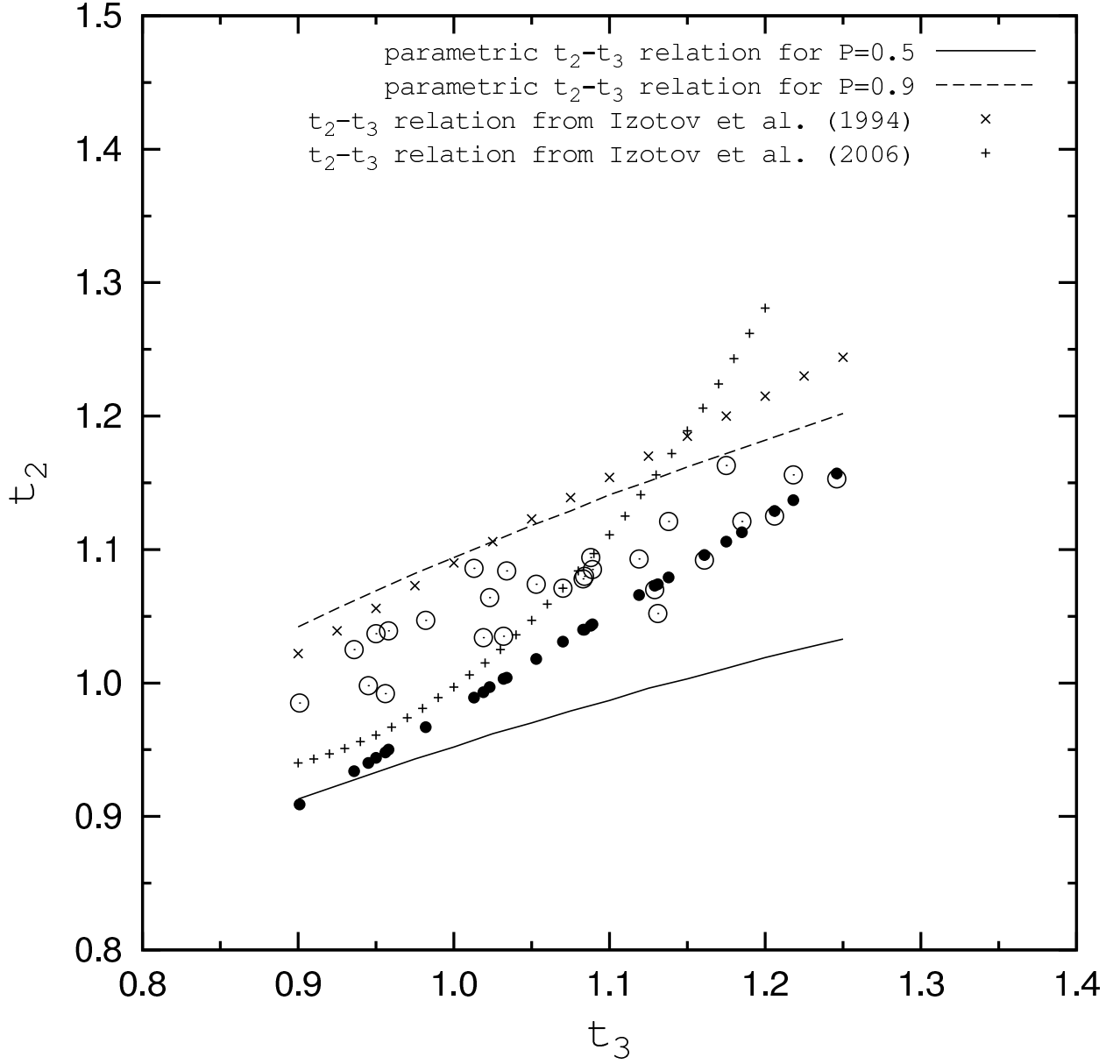


Fig. 9.— The $t_2 - t_3$ diagram. Open and filled circles denote HII regions with t_2 derived respectively with the two-dimensional parametric and one-dimensional $t_2 - t_3$ relations. The curves corresponding to the parametric relation are shown for two different values of the excitation parameter, $P = 0.5$ (solid line) and $P = 0.9$ (dashed line). The $t_2 - t_3$ relations from Izotov et al. (1994) and Izotov et al. (2006) are shown respectively by crosses and plus signs.

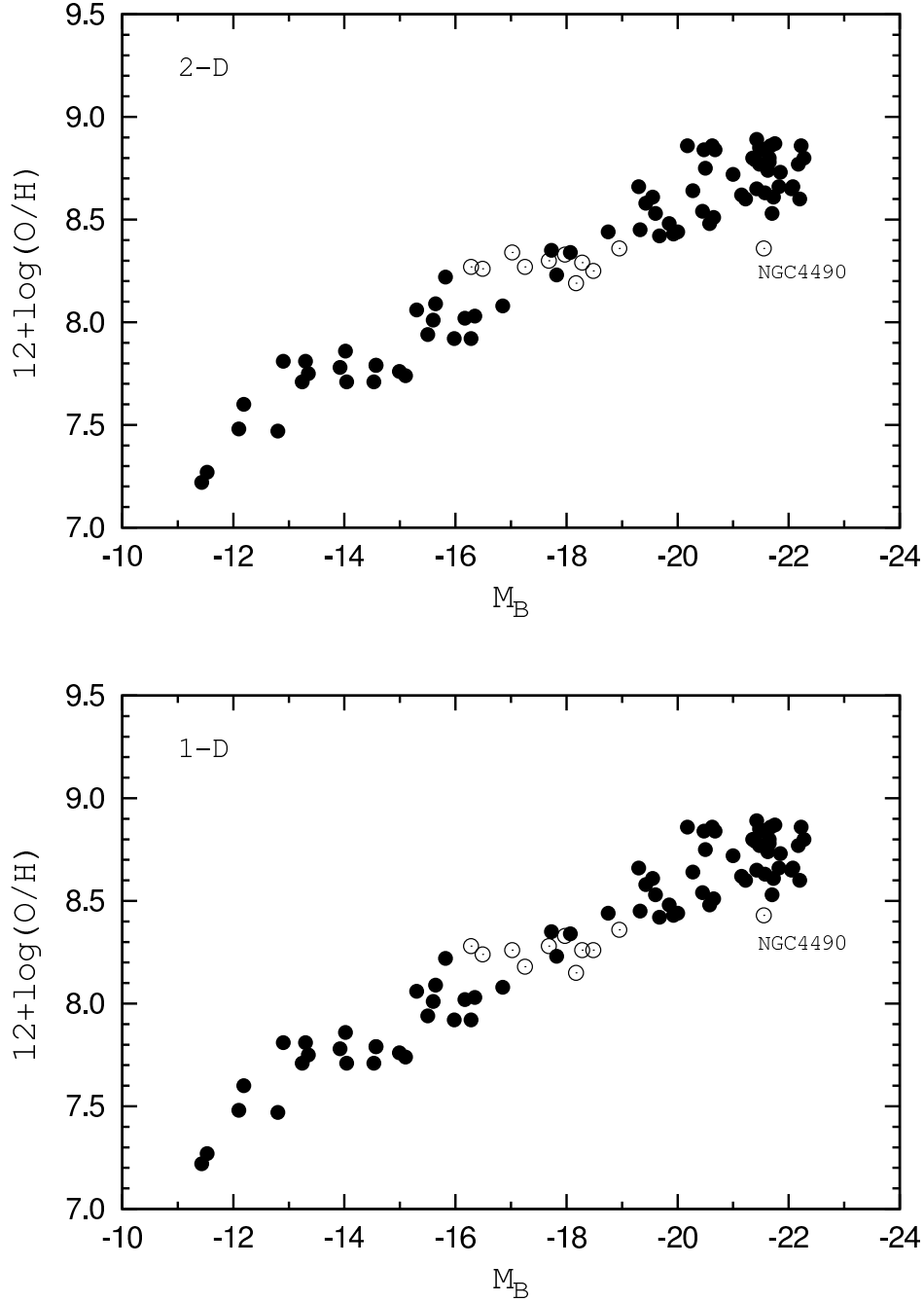


Fig. 10.— The luminosity – central metallicity diagram. *Top panel.* The open circles show the galaxies in Table 4, with abundances determined with the parametric $t_2 - t_3$ relation. The filled circles show data from Pilyugin et al. (2007). *The bottom panel.* The same as in the top panel, except the abundances of the galaxies in Table 4 have been determined with the one-dimensional $t_2 - t_3$ relation.